The Pennsylvania State University

The Graduate School

College of Engineering

DESIGN AND DEVELOPMENT OF A 30-GHz MICROWAVE ELECTROTHERMAL THRUSTER

A Thesis in

Aerospace Engineering

by

Erica E. Capalungan

Submitted in Partial Fulfillment
of the Requirements
for the Degree of

Master of Science

August 2011

The thesis of Erica E. Capalungan was reviewed and approved* by the following:

Michael M. Micci
Professor of Aerospace Engineering
Director of Graduate Studies
Thesis Advisor

Sven G. Bilén
Associate Professor of Engineering Design, Electrical Engineering, and Aerospace Engineering

George A. Lesieutre
Professor of Aerospace Engineering
Head of the Department of Aerospace Engineering

*Signatures are on file in the Graduate School.

ABSTRACT

Research has been conducted on the microwave electrothermal thruster at The Pennsylvania State University since the 1980's. Each subsequent thruster incorporated modifications that resulted in improvements in thruster performance compared to previous generations. Operational frequencies evaluated thus far include 2.45 GHz, 7.5 GHz, 8 GHz, and 14.5 GHz. As each thruster increased in operational frequency, plasmas have been ignited with successively lower amounts of input power. With higher frequency and lower power requirements, the physical sizes of the thruster and the power supply have been reduced. Decreased size results in a lighter propulsion system, which is ideal for space missions. This thesis concerns the design and development of a thruster operating at 30 GHz.

Electromagnetic modeling was used in the design of the thruster to determine the optimal input antenna size and length. A 2.4-mm antenna size was chosen with a length that is flush with the bottom of the cavity. Modeling also aided in the understanding of how machining accuracy of the cavity radius affects thruster performance. The modeling results indicated that radius inaccuracies on the order of ±0.1 mm result in mode distortion, shifting of the resonant frequency, lowered electric field strength, and poor power transfer to the cavity.

The experimental setup for the thruster system, propellant system, electromagnetic system, and pressure system are discussed. The 30-GHz MET has an approximate radius of 0.4 cm and height of 1.4 cm. The expected power requirement for plasma ignition is 5–10 watts. Scaling down the thruster size resulted in different adapters and enhanced pressure sealing requirements when compared to previous METs. Initial testing is being performed at a pressure of 30 Torr using helium as the propellant. A network analyzer was used to determine the exact resonant frequency of the cavity and to determine the power coupling to the cavity. The exact resonant frequency of the cavity is 29.939 GHz. The initial setup of the thruster indicated a power coupling of 6 dB while reducing the length of the antenna resulted in enhanced power coupling of at least 25 dB. The fabrication and testing of this thruster gave rise to many design improvements that are also discussed.

TABLE OF CONTENTS

LIST OF FIGURES

LIST OF TABLES

NOMENCLATURE

A_e	Nozzle Exit Area, m^2	L	Characteristic Length, m
a	Cavity Radius, m	$\dot{m}$	Mass Flow Rate, kg/s
$\mathbb{A}$	Magnetic Vector Potential, H·A/m	M_i	Initial Spacecraft Mass, kg
$\mathcal{B}$	Instantaneous Magnetic Flux Density, Wb/m^2	M_f	Final Spacecraft Mass, kg
B_{mn}	Vector Potential Constant, H·A/m	$\mathcal{M}_i$	Source Magnetic Current Density, V/m^2
$\mathcal{D}$	Instantaneous Electric Flux Density, C/m^2	N_D	Particle Number Density
$\mathcal{E}$	Instantaneous Electric Field Intensity, V/m	P	Power, W
$\mathbb{E}$	Complex Electric Field Intensity, V/m	P_a	Ambient Pressure, Pa
E_{ion}	Ionization Energy	P_{ave}	Average Power, W
f	Frequency, Hz	P_e	Nozzle Exit Pressure, Pa
$\mathbb{F}$	Electric Vector Potential, V	P_{inc}	Incident Power, W
g	Gravitational Acceleration, m/s^2	P_{ref}	Reflected Power, W
$\mathcal{H}$	Instantaneous Magnetic Field Intensity, A/m	q	Charge of Particle, C
$\mathbb{H}$	Complex Magnetic Field Intensity, A/m	q_{ev}	Electric Charge Density, C/m^3
h	Cavity Height, m	q_{mv}	Magnetic Charge Density, Wb/m^3
I_{sp}	Specific Impulse, s	RL	Return Loss, dB
J_i	Source Electric Current Density, A/m^2	U_e	Exhaust Velocity, m/s
J_m	Bessel Function	U_{eq}	Equivalent Exhaust Velocity, m/s
J'_m	First Derivative of Bessel Function	ΔU	Change in Velocity
$V_{0,\text{inc}}$	Incident Voltage, V	Z_L	Load Impedance

Z_0	Characteristic Impedance
β	Phase Constant
β_ρ	Phase Constant in ρ-Direction
β_z	Phase Constant in z-Direction
ε	Permittivity, F/m
η	Efficiency
Γ	Voltage Reflection Coefficient
λ_D	Debye Length, m
μ	Permeability, H/m
ρ	Density, kg/m^3
σ	Conductivity, S/m
τ	Thrust, N
τ_c	Mean Time Between Collisions, s
χ_{mn}	Zeros of the Bessel Function
ω	Field Radian Frequency, rad/s
ω_c	Frequency of Collisions, s^{-1}

ACKNOWLEDGMENTS

I would like to take this time to recognize the many people that have helped me throughout my graduate studies. First and foremost is Dr. Micci for the guidance he provided in every problem I encountered and the confidence he had in me especially during the challenging parts of my research. To Dr. Bilén for the wealth of knowledge he provided and his enthusiasm for electric propulsion, which he shared with all of his students. Thank you to Mr. Dillon for his machining skills and manufacturing knowledge. To Mr. Robert Capuro and Dr. Vladimir Getman for all the spare time and help they provided me in troubleshooting equipment failures. Thanks to Peter Hammond and Jeff Hopkins for their guidance and company while working in the lab. Also thanks to my fellow aerospace electric propulsion research friends for their weekly insight and ideas into advancing my research.

On a more personal note, I could not have accomplished this without the love and support of my family and friends. Finally, I would like to thank Scott for listening, providing advice, and aiding me when needed for not only my graduate studies but also throughout life as well.

CHAPTER 1

INTRODUCTION

Research on the microwave electrothermal thruster (MET) at The Pennsylvania State University has been ongoing since the early 1980's. The overall goal for the MET research is to develop an efficient and reliable form of electric propulsion for use in space. Research has primarily been experimental, but also more recently has included numerical and computational modeling of the thruster physics. Thrusters operating at different frequencies have been designed and successfully tested with a variety of propellants and chamber pressures. The first thruster developed at Penn State operated at a frequency of 2.45 GHz; subsequent research explored higher frequencies of operation: 7.5 GHz, 8 GHz and 14.5 GHz. By increasing the frequency of the thruster and thereby decreasing the size, plasma generation can occur at lower input power with increased performance. This thesis concerns the design and development of the MET at a frequency of 30 GHz.

1.1 Space Propulsion Overview

1.1.1 Categorization of Rocket Propulsion

Propulsion systems are used throughout the world today in cars, trains, airplanes, and spacecraft. The basic idea behind a reaction propulsion device is to exhaust mass, usually in the form of a high temperature gas, creating thrust. This idea follows from Newton's Third Law: for every action there is an equal and opposite reaction. For the purpose of this thesis, we will direct our attention specifically to space propulsion. Space propulsion devices can be used in applications such as launch, orbital maneuvering, attitude control, and interplanetary missions, to name a few. Space propulsion can be categorized into five broad areas: chemically powered, electrically powered, physically powered, thermally powered, and powered via nuclear means.

Physically powered, thermally powered, and powered via nuclear means are not common forms of space propulsion. Examples of physically powered propulsion devices are cold gas thrusters and water rockets. Both use non-chemically reacting propellants. Examples of thermally powered thrusters are solar and beamed thermal thrusters. Solar thermal thrusters use solar energy to directly heat a propellant, whereas beamed thermal thrusters use beamed energy to heat a propellant. Nuclear thrusters utilize a nuclear reaction as the power source for the thruster.

The most common forms of space propulsion are chemical and electric propulsion. Chemical propulsion has the longest history of development and reliability. Chemical rockets exploit the chemical bonds of the propellant, the energy source for the thruster. There is a finite amount of energy that can be obtained from chemical bonds, which leads to the classification of chemical rockets as energy-limited devices. This category of propulsion can be discretized further into liquid, solid, and hybrid rockets. Liquid rockets consist primarily of monopropellants and bipropellants. Solid rockets consist of a fuel and oxidizer combination. Hybrid rockets have attributes associated with both liquid and solid rockets. Chemical rockets are capable of achieving large amounts of thrust when compared to other forms of propulsion. The specific impulse of the rocket depends primarily on the composition of the propellant and the chamber temperature. Chemical rockets require heavy propellants and the maximum chamber temperature attainable from chemical bonds is limited. Due to these reasons, chemical rockets have specific impulses in the range of 400 to 450 seconds, which is low when compared to electric thrusters.[1]

Electrically powered thrusters are becoming more common on satellites for attitude control and orbital maneuvering. They are also used more frequently for interplanetary missions due to their high efficiency at using propellant mass. By either electrically heating or using electric and/or magnetic fields to accelerate a gas, thrust is generated without the thermal limitations of chemical rockets. The use of electric and magnetic forces to accelerate particles translates to lighter propellant options, further decreasing the mass of the propellant required on board. Specific impulses for electric propulsion devices have achieved values up to 10,000 seconds.[1] Theoretically, there is no limit to the amount of energy that can be extracted using electric propulsion but there is a practical limitation on the amount of power available. For this reason, electric propulsion devices are known as

power-limited devices. In contrast to chemical propulsion devices, electric propulsion requires a power source. The power can be obtained in a variety of manners, such as solar, nuclear, or beamed energy. Electric thrusters are discretized further into three categories: electrostatic, electromagnetic, and electrothermal thrusters.

Electrostatic thrusters utilize electric fields to accelerate charged particles. The requirement of charged particles in the system requires an ionization source. Due to the characteristics of electrostatic devices, there is no limit on the exhaust velocity; however, there is a limit on the mass flux due to space-charge effects.[2] To prevent positively charged particles from being attracted back to the spacecraft, exhaust neutralization is required. By emitting the same number of electrons as the number of ions being expelled, the exhaust is neutralized. This is often done by using an electron gun, hollow cathode, thermionic emitter, or field emitter. These propulsion devices are meant to be turned on for long periods of time.

Examples of electrostatic thrusters are ion and Hall thrusters. The ion thruster is the most fully developed electric propulsion device and as such has a longer history of space flight and more technical literature. The basic principle is to accelerate ions across an electrostatic field created by a potential drop across grids, as seen in Figure 1.1.

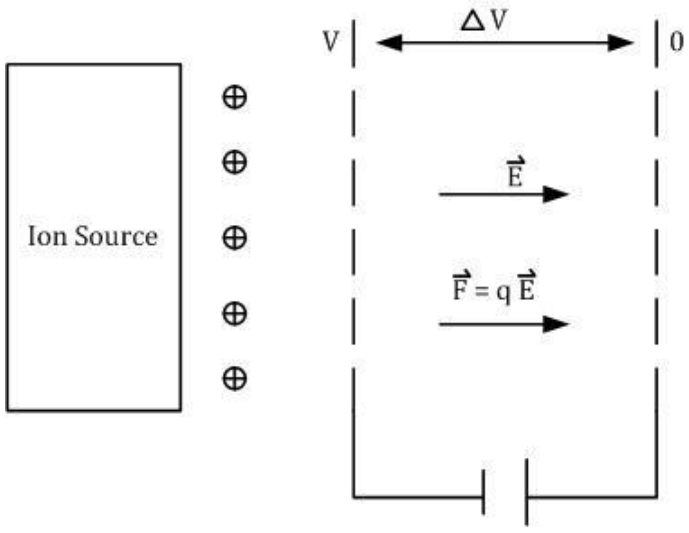

Figure 1.1: Diagram of Electrostatic Thruster Operation.

Electromagnetic thrusters use a combination of electric and magnetic fields, steady or transient, to accelerate a plasma. Electromagnetic propulsion devices can be broken into

two categories, steady and unsteady. Steady electromagnetic devices generate a current and pass it through a magnetic field to create the force seen in Figure 1.2.

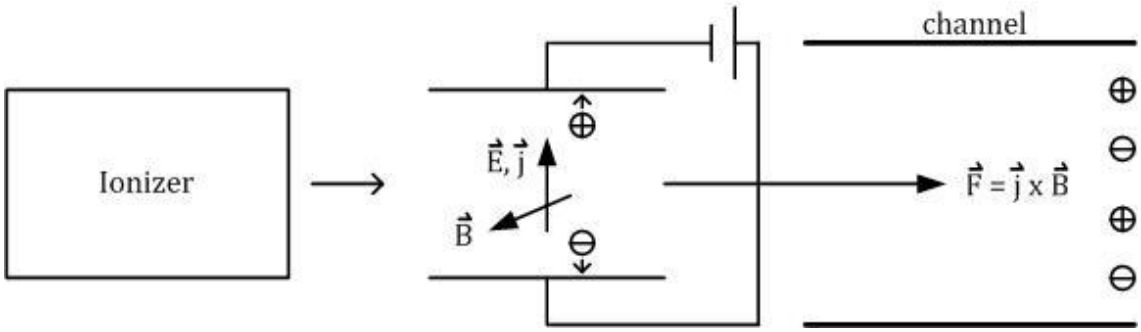

Figure 1.2: Diagram of Electromagnetic Thruster Operation.

Disadvantages of electromagnetic thrusters are the required ionization energy, the need for a strong magnetic field, and channel erosion.[2] An example of a steady electromagnetic thruster is the magnetoplasmadynamic thruster (MPD). In a MPD, a current is generated between the anode and the cathode. The propellant is ionized as it passes through the current. The strong current generates a magnetic field, which creates a force felt by the ionized particles. Examples of unsteady, or transient, electromagnetic thrusters are the pulsed plasma thruster and pulsed inductive thruster. For both thrusters, a current is generated and an arc forms at the point of lowest inductance in the circuit. The current flow generates a magnetic field, which in turn generates a force propelling the arc down a channel.

Electrothermal thrusters use electrical or electromagnetic energy to heat the propellant before expanding it through a nozzle to generate thrust. This form of electric propulsion is similar in operation to chemical rockets. The difference is, by using electrical energy instead of a chemical reaction, higher chamber temperatures and lower molecular weights are obtained, thereby increasing the exhaust velocity.[2] Examples of electrothermal thrusters include resistojets, arcjets, RF thrusters, and microwave thrusters. The resistojet uses electrical resistance to heat the propellant and then expands it through a nozzle. An example of a resistojet basic operation is shown in Figure 1.3. The inherent disadvantage of the resistojet is the thermal limitations imposed by resistance heating; the propellant can only get as hot as the heating element and the heating element is limited by the element's melting temperature. The arcjet heats the gas directly by using an electrical arc, as seen in

Figure 1.3. Cathode erosion is the primary limitation of the arcjet. The start-up process is highly erosive, which makes this thruster unsuitable for attitude control. RF thrusters use RF energy to generate a plasma that heats the propellant. The RF thruster creates a plasma that fills the entire thruster chamber, which results in temperature loss through the walls. Microwave thrusters use microwave energy inside of a resonant cavity to create a standing wave concentrating the electric field to a point. The electric field breaks down at the point of highest concentration, forming a free-floating plasma. The propellant is thermally heated as it passes through the plasma. By specifying the cavity dimensions, the point of plasma formation can be chosen to be close to the nozzle entrance. This allows the maximum amount of propellant to be heated while minimizing heat loss through the walls.

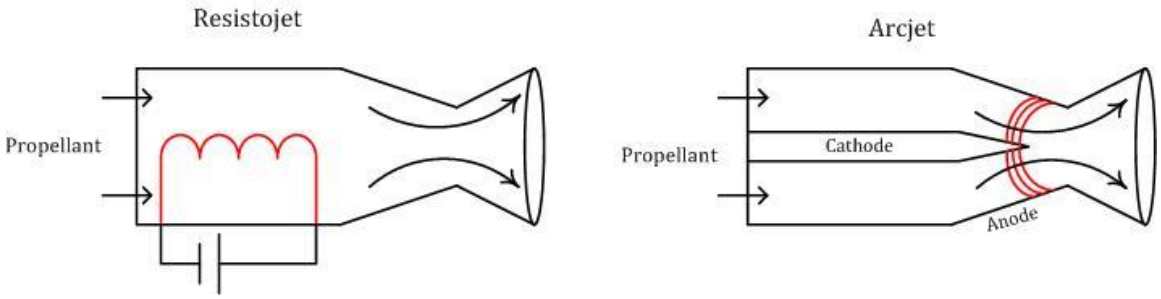

Figure 1.3: Examples of Electrothermal Thrusters.

1.1.2 Performance Characterization of Rocket Propulsion

There are several key parameters used to characterize the performance of rocket engines. One of the most widely known is thrust, τ. Thrust can be explained through the use of Newton's Third Law and conservation of momentum. Newton's Third Law states that for every action there is an equal and opposite reaction. Thrust is the reaction force felt due to the acceleration of mass in a given direction. Quantitatively, the equation for thrust can be derived through conservation of momentum across the surface of a control volume. Conservation of momentum states that the net force is equal to the change in momentum across the control volume surface. Figure 1.4 displays the most important forces involved in the control volume analysis.

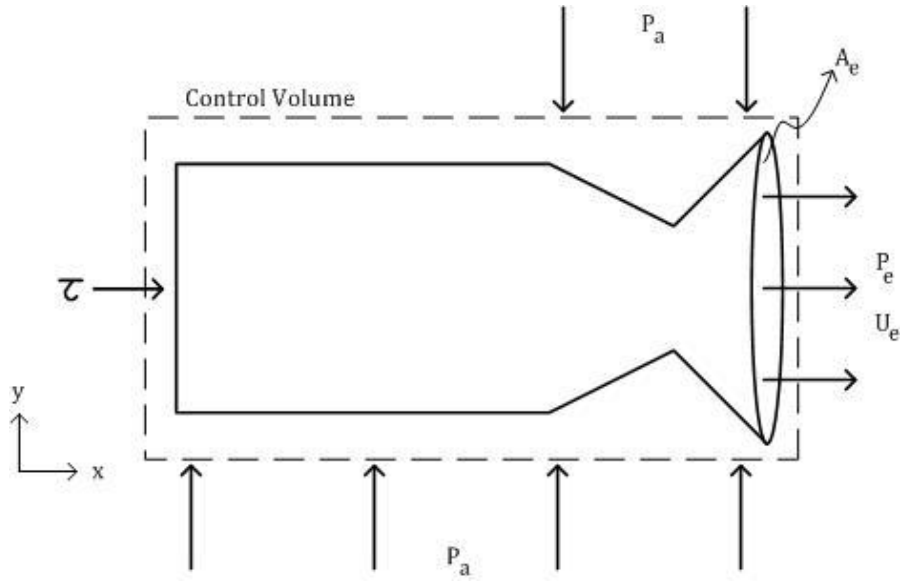

Figure 1.4: Force Analysis on Thruster Control Volume.

The thrust and the pressure gradient are the forces acting on the control volume, and the sum of these forces may be written[1]

$$\sum F = \tau + (P_a - P_e)\, A_e. \tag{1.1}$$

Because there is no mass flux into the control volume, the momentum into the control volume is zero. The momentum out of the control volume is equal to the mass flux out of the control volume multiplied by the velocity at which it is exiting. Combining these quantities and rearranging provides the equation used to determine thrust: [1]

$$\tau = \dot{m}\, U_e + (P_e - P_a)\, A_e. \tag{1.2}$$

A key parameter in the determination of thrust is the exhaust velocity, U_e. The equivalent exhaust velocity, U_{eq}, is used to express thrust as a change in propellant momentum only and is defined as[1]

$$U_{\text{eq}} = U_e + \frac{(P_e - P_a)\, A_e}{\dot{m}}. \tag{1.3}$$

Substituting Equation 1.3 into Equation 1.2 results in a simplified equation for thrust:[1]

$$\tau = \dot{m} \cdot U_{\text{eq}}. \tag{1.4}$$

Also, by invoking conservation of momentum, the "Rocket Equation" can be derived:[1]

$$\Delta U = U_e \ln\left(\frac{M_i}{M_f}\right). \tag{1.5}$$

This leads to three key advantages of having a higher exhaust velocity. First, for the same amount of propellant the thruster will have a longer service life. Second, lower propellant mass allows for more payload capacity. Third, lower propellant and same payload requires a smaller launch vehicle.

Another metric in the evaluation of thruster performance is the specific impulse, [1]

$$I_{\text{sp}} = \frac{\tau}{\dot{m}\, g} = \frac{U_{\text{eq}}}{g}. \tag{1.6}$$

The specific impulse is a way of expressing the efficiency of the thruster with unit of time. As an example of how I_{sp} is related to efficiency and propellant mass requirements, Table 1.1 lists the propellant mass required for a number of thrusters to provide north–south station-keeping control. The thrusters are to provide station keeping for ten years on a 2270 kilogram satellite.[3] In the table is a list of the specific impulse, propellant mass and propellant mass fraction for four types of thrusters.

Table 1.1: Comparison of Chemical and Electrical Efficiency and Propellant Mass.[2]

Thruster	**Monopropellant**	**Bipropellant**	**Microwave Heated**	**Ion Engine**
Specific Impulse	250 s	300 s	600 s	2800 s
Propellant Mass	419 kg	355 kg	185 kg	41 kg
Propellant Fraction	18.5%	15.6%	8.15%	1.81%

As the specific impulse of the thrusters in Table 1.1 increases from left to right, the required propellant mass decreases. The decrease in propellant mass reduces the ratio of propellant

mass to total mass as seen in the propellant fraction. The concept of specific impulse in relation to efficiency leads us to define efficiency, η, for electric propulsion devices:[1]

$$\eta = \frac{\text{Power Out}}{\text{Power In}} = \frac{\frac{1}{2}\,\dot{m}\,U_e^2}{\frac{1}{2}\,\dot{m}\,U_e^2 + E_{\text{ion}}}. \tag{1.7}$$

The power out of the system is the kinetic energy created by the thruster. The efficiency of an electric propulsion device is highly dependent on the ionization energy required, E_{ion}. Equation 1.7 indicates that increasing the exhaust velocity can also increase the efficiency of the thruster.

Thrust, exhaust velocity, and power of the electric thruster are interdependent as shown in the relationship for input power required: [1]

$$P = \frac{\tau\,U_e}{2\,\eta} = \frac{\tau\,g\,I_{\text{sp}}}{2\,\eta}. \tag{1.8}$$

By analyzing Equation 1.8, one can see that, for a fixed input power, P, the product of thrust and specific impulse is also fixed. If the mission requires an increase in thrust, then there would be a subsequent decrease in the specific impulse and vice versa. This also shows that, theoretically, there is no upper limit to thrust and specific impulse. However, there is a practical limit to the amount of available power on the spacecraft to achieve the thrust and specific impulse.

1.2 Motivation for Electric Propulsion

The motivation for electric propulsion stems from the need for higher exhaust velocities than can be achieved by simple chemical propulsion. Electric propulsion devices remove the thermal limitations inherent to chemical propulsion devices. Propulsion systems for planetary missions require a high degree of reliability, efficiency, and exhaust velocity. Through the use of electric propulsion, all of these requirements can be satisfied. By increasing the exhaust velocity, the specific impulse and efficiency of the thruster also

increase. Higher efficiency translates to longer flight duration, a must for interplanetary missions. Another benefit to electric propulsion is the increased variety of propellants available.

1.3 MET Overview

1.3.1 Design and Operational Overview

The MET operates by heating a propellant with a microwave-generated, free-floating plasma. The propellant is exhausted through a gas-dynamic nozzle to generate thrust. The thruster consists of a cylindrical cavity that is geometrically sized to create a standing wave, focusing the electric field at several locations in the cavity. The electric field breaks down the gas where the electric field strength is highest, forming a free-floating plasma in a properly dimensioned and designed cavity. The MET operates in the TM_{011}^{z} mode. This mode concentrates the electric field at the ends of the cavity and the midplane as seen in Figure 1.5.

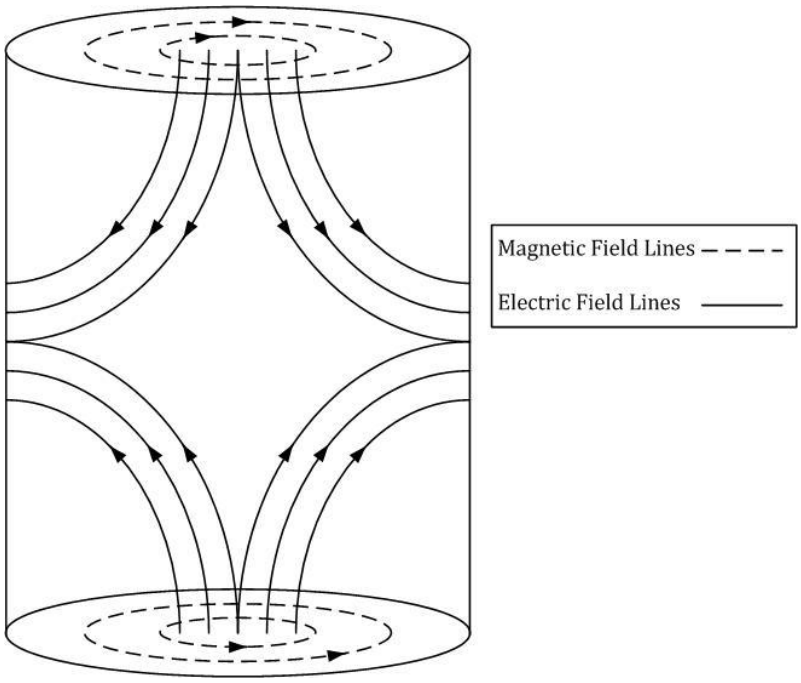

Figure 1.5: Electric and Magnetic Field Lines for the TM_{011}^{z} Mode.

By sizing the cavity correctly and concentrating the electric field at its ends, a plasma can be created near the entrance to the nozzle. This is the ideal location for the plasma to form because it allows for the most thermal energy transfer to the propellant by the plasma. The basic layout of the MET is shown in Figure 1.6.

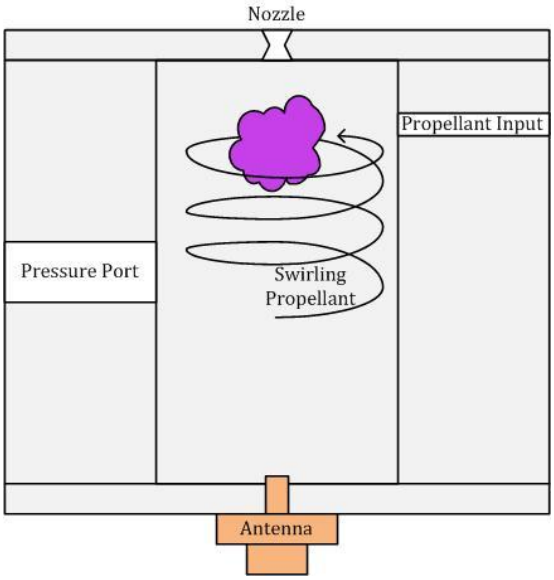

Figure 1.6: Basic Operational Layout of the MET.

The two ends of the cavity are conductive plates. The antenna is located at the bottom and the nozzle is located at the top. The microwave energy enters the cavity through an antenna chosen specifically for the cavity dimensions and operating frequency. The propellant enters the cavity tangentially and near the nozzle entrance. This entrance method is chosen for two reasons. First, the tangential entrance creates a swirling effect acting as a means of cooling the thruster walls. Second, the plasma is stabilized along the center of the cavity. The heated propellant exits through a converging–diverging nozzle to create thrust. The pressure port is present to allow for internal pressure measurements during operation.

The plasma is ignited at low pressures—at pressures below 50 Torr—and sustained at higher pressures. The MET has several advantages over other electric propulsion devices. One advantage is the absence of an electrode, the main component that limits the lifetime of arcjets. Another advantage is the free-floating plasma. By removing contact between the plasma and the walls, there is less thermal heat loss and less material erosion. Another less obvious advantage is the freedom in the design of the thruster. The cavity geometry,

position of the plasma, propellant flow rate, and flow configuration can all be easily varied to yield the desired performance requirements.[4]

1.3.2 Prior Experimental Research

Research on the MET began in the 1980's at The Pennsylvania State University with 2.45 GHz as the first frequency of investigation. Nitrogen and helium plasmas were generated in the TM_{012}^{z} mode with powers up to 400 W.[5] The research progressed to other propellants and higher input powers.

The investigation of waveguide-heated plasmas at 2.45 GHz began in order to understand their operational characteristics. Observations of the rectangular waveguide generated plasmas in a TE_{10} mode showed physical contact between the plasma and the waveguide walls resulting in efficiency losses.[6] It was through this research that the transition from the TE_{10} mode to a circular TM_{01} mode was evaluated.[6] By transitioning to the TM_{01} mode, the generated plasma was more stable and did not interfere with the waveguide walls. This resulted in much higher coupling efficiencies.[6] The following performance values were estimated for the thruster: thruster efficiency of 40 percent, specific impulse of 350 s, and thrust of 0.4 N.[6]

Experimental research comparing the coupling efficiencies and stabilization of the TM_{011} and TM_{012} modes resulted in bluff body and swirling flow stabilization schemes.[7] Through this experimental research and comparisons with previous numerical research, the next generation thruster was designed for plasma formation concentrated near the nozzle entrance and tangential propellant input.[8] The thruster was successfully operated with multiple propellants: helium, nitrogen, hydrogen, and ammonia.[8] The thruster was also operated for extensive periods of time with input powers of 2200 W.[8] Microwave power coupling efficiencies were above 97 percent.[8] The 2.45-GHz MET is shown firing in Figure 1.7.

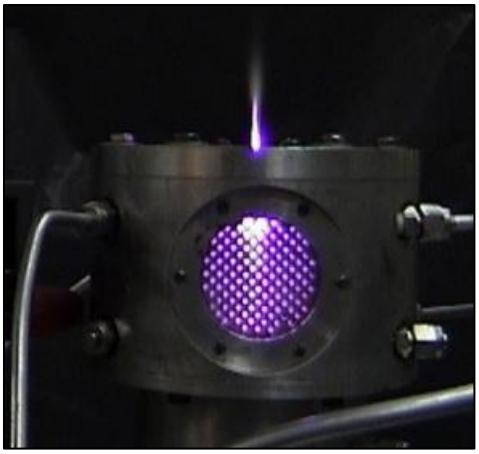

Figure 1.7: Operation of the 2.45-GHz MET.

The development of a higher frequency thruster began in the 1990's with an operational frequency of 7.5 GHz. The thruster was designed for an input power of 100 W and required a new thrust stand.[9]

Through the late 1990's, the investigation on the 2.45-GHz and 7.5-GHz thrusters continued with a goal of comparing the performance of the two thrusters.[10] Using helium, nitrogen, and ammonia propellants at power levels up to 100 W, the two devices were tested in simulated space conditions.[10] The successful creation and maintenance of plasmas at low power levels in simulated space conditions was demonstrated.[10]

Clemens' research on the 7.5-GHz thruster used three nozzles with different throat diameters to analyze the relationship between mass flow and chamber pressure.[11] It was concluded that the performance of the 7.5-GHz MET improved with increasing chamber pressure and mass flow.[11] Modifications to the momentum-trap thrust stand were made to allow for more accurate thrust measurements on this low power thruster.[11] The 7.5-GHz MET is shown firing in Figure 1.8.

Figure 1.8: 7.5-GHz MET Firing Helium in Vacuum Conditions.

In an attempt to further reduce the power, mass, and size requirements, a redesign of the 7.5-GHz MET was completed for an operating frequency of 14.5 GHz. The 14.5-GHz MET was designed to operate with a maximum input power of 20 W.[12] Further improvements were made to the tangential propellant input and a dielectric insert was investigated as a means of plasma confinement, as opposed to the dielectric separation plate that had been employed previously in lower frequency cavities.[12] Plasma ignition was successful but the thruster performance was poor due to the adverse effects of the dielectric insert on the electromagnetic fields.[12]

Continued research on the 14.5-GHz MET analyzed the antenna design, RF inputs, and dielectric shape.[12] Design modifications resulted in increased power handling, plasma ignition repeatability, and stabilization of the plasma.[13] The increase in forward power to 100 W resulted in an increase in thrust from 4.2 mN, obtained by Goovaerts, to 11.33 mN.[12,13] Coupling efficiencies of 96 percent were also obtained.[13] The 14.5-GHz MET can be seen operating in Figure 1.9 below.

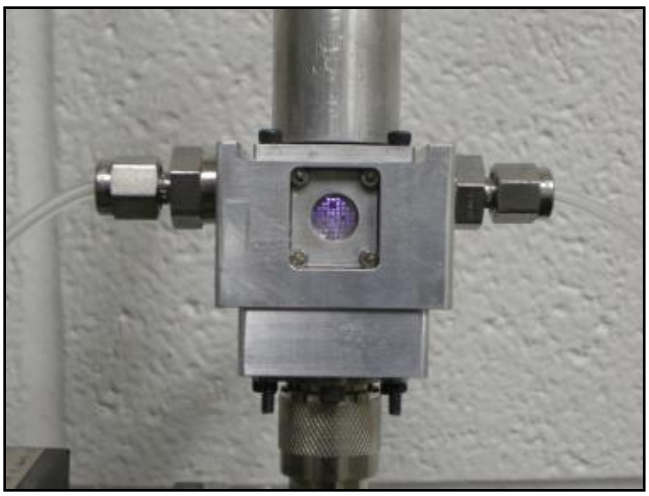

Figure 1.9: 14.5-GHz MET Firing Helium in Simulated Vacuum Conditions.[13]

In the last decade, research also began on a thruster operating at 8 GHz. The chamber was designed around the operating specifications of a space-rated TWTA power supply.[14] The thruster was scaled down from the 7.5-GHz MET and was intended for use at a maximum of 350 W input power.[14] Successful thruster configuration and optimum propellant choice resulted in specific impulses greater than any other MET tested using ammonia.[14] Research at The Pennsylvania State University continues on the optimization of this thruster.

1.3.3 Prior Numerical Research

In an attempt to minimize costs associated with experimental research, numerical electromagnetic modeling has been used for the last ten years. The electromagnetic design of the thruster is complex, but important to the performance of the MET. COMSOL Multiphysics (previously called FEMLAB), has been used to model the cavity environment.[15] COMSOL Multiphysics simultaneously solves the equations involved in the thermal dynamics and electromagnetics of the cavity.[15] Different cavity configurations were evaluated and frequency sweeps were performed to determine the resonant frequencies of the cavities.[15] This modeling aided in the optimization of the 7.5-GHz MET and proved to be a valuable means of quickly increasing performance of the thruster.[15]

Further computational studies were performed on the 7.5-GHz MET to analyze the fluid dynamics of the thruster in addition to the electric fields of the TM_{011}^{z} resonant mode.[16] The

electric field analysis provided insight into changes of electric field strength and resonant frequency due to the size and shape of the antenna, the nozzle geometry, and different dielectric configurations.[16] Results from the evaluation of the antenna's size and shape indicated the presence of resonant frequency shifts.[16] Nozzle geometry did not affect the overall strength of the electric field but it did affect the location of maximum field strength.[16] Introducing a dielectric material into the resonant cavity affects the resonant frequency. As expected, this modeling indicated that an increase in dielectric material shifts the resonant frequency down and the field strength is directly related to the amount of dielectric material.[16] The computational fluid dynamic studies were used to predict thrust, chamber pressure, and mass flow rates.[16]

The most recent numerical modeling evaluated the design of the 8-GHz MET. The objective was to create a complete numerical model of the fluid mechanics, thermodynamics, plasma physics, and electromagnetics of the thruster.[17] Electromagnetic modeling using COMSOL Multiphysics was performed to obtain a strong electric field near the nozzle entrance by optimizing the TM_{011}^{z} mode.[17] The propellant injection system was analyzed using incompressible and weakly compressible fluid flow assumptions.[17]

1.4 Motivation for a 30-GHz MET

Previous research has shown that by increasing frequency, thereby decreasing thruster size, a plasma can be created with lower input power. By utilizing a higher frequency, the thruster decreases in mass and physical size allowing room for more payload or smaller launch vehicles. To package a propulsion system small enough to be used on a 3U CubeSat, for example, would greatly expand the mission capabilities of the CubeSat platform. Also, by increasing the operational frequency, the power requirements for the propulsion system decrease. If the propulsion system uses less power, this can translate to a lighter power supply or it can allow the excess power to be used by other subsystems onboard the spacecraft.

1.5 Thesis Overview

Throughout the remaining portions of this thesis, the design, development, and fabrication of the 30-GHz MET are discussed. Chapter 2 discusses the theory behind the operation and performance of the MET. The electromagnetic theory and the plasma physics of the thruster are analyzed. Chapter 3 presents the design considerations of the thruster with an overview of the COMSOL Multiphysics modeling setup. The results and discussion of the modeling and manufacture of the thruster are provided in Chapter 4, while the experimental setup and preliminary testing are in Chapter 5. Finally, the conclusions, recommendations, and future work are presented in Chapter 6.

CHAPTER 2

THEORY

2.1 Electromagnetic Theory

The study of electromagnetic theory and microwave engineering is essential to the understanding of the microwave electrothermal thruster. The microwave energy introduced to the cavity creates the plasma in order to heat the propellant.

The electromagnetic spectrum is arranged based on signal frequency. The microwave region of the electromagnetic spectrum consists of the frequencies between 0.3 and 300 GHz. The wavelengths associated with this region of frequencies makes standard circuit theory inadequate; therefore, another means of analyzing the electric and magnetic fields in the microwave region are needed. James Maxwell is credited as the founder of modern electromagnetic theory. Maxwell's equations act as a set of governing equations that relate magnetic and electric fields.

2.1.1 Deriving the Wave Equations

To begin the process of understanding the electric and magnetic fields inside of the MET, we show how the wave equations are derived from Maxwell's equations. The electric and magnetic fields for a boundary value problem, such as the MET, can be obtained using either Maxwell's Equations or the uncoupled, second-order partial differential equations known as the wave equations. For our purposes, the vector wave equations will be used to obtain the electric and magnetic field solutions.

The four equations known as Maxwell's equations in differential form are

$$\nabla \times \mathcal{E} = -\mathcal{M}_i - \mu \frac{\partial \mathcal{H}}{\partial t}, \tag{2.1a}$$

$$\nabla \times \mathcal{H} = J_i + \sigma \mathcal{E} + \varepsilon \frac{\partial \mathcal{E}}{\partial t}, \tag{2.1b}$$

$$\nabla \cdot \mathfrak{D} = q_{ev}\,, \tag{2.1c}$$

$$\nabla \cdot \mathcal{B} = q_{mv}\,. \tag{2.1d}$$

Equations 2.1a and 2.1b are the uncoupled form of Faraday's Law and Ampere's Law, respectively. Equations 2.1c and 2.1d are known as Gauss' Law and Gauss' Law for Magnetism, respectively. By assuming a source-free region, the vector wave equations for $\mathcal{E}$ and $\mathcal{H}$ can be derived and are[18]

$$\nabla^2 \mathcal{E} = \mu\, \sigma \frac{\partial \mathcal{E}}{\partial \mathrm{t}} + \mu\, \varepsilon \frac{\partial^2 \mathcal{E}}{\partial \mathrm{t}^2}, \tag{2.2a}$$

$$\nabla^2 \mathcal{H} = \mu\, \sigma \frac{\partial \mathcal{H}}{\partial \mathrm{t}} + \mu\, \varepsilon \frac{\partial^2 \mathcal{H}}{\partial \mathrm{t}^2}. \tag{2.2b}$$

Assuming a lossless media, where $\sigma = 0$, the wave equations can be further reduced to the following[18]

$$\nabla^2 \mathcal{E} = \mu\, \varepsilon \frac{\partial^2 \mathcal{E}}{\partial \mathrm{t}^2}, \tag{2.3a}$$

$$\nabla^2 \mathcal{H} = \mu\, \varepsilon \frac{\partial^2 \mathcal{H}}{\partial \mathrm{t}^2}. \tag{2.3b}$$

Equations 2.3a and 2.3b can be written in time-harmonic form, where the time variations are of the form $e^{j\omega t}$, and ω represents frequency of the waves. This is done by replacing the second-order time derivative with $(j\omega)^2$ and the instantaneous electric and magnetic fields with their complex counterparts, i.e,

$$\frac{\partial^2}{\partial t^2} \rightarrow (j\omega)^2 = -\omega^2$$

$$\mathcal{E}, \mathcal{H} \rightarrow \mathbb{E}, \mathbb{H}$$

The variables β and ω are the phase constant with units of radians per meter and the field radian frequency with units of radians per second, respectively, and are related by

$$\beta^2 = \omega^2 \mu \varepsilon. \tag{2.4}$$

With these substitutions, the wave equations can be simplified to the following set of equations:[18]

$$\nabla^2 \mathbb{E} = -\beta^2 \mathbb{E}, \tag{2.5a}$$

$$\nabla^2 \mathbb{H} = -\beta^2 \mathbb{H}. \tag{2.5b}$$

The MET is a cylindrical cavity and, as such, the field solutions are easier to derive in a cylindrical coordinate system. The components of the cylindrical coordinate system are shown in Figure 2.1.

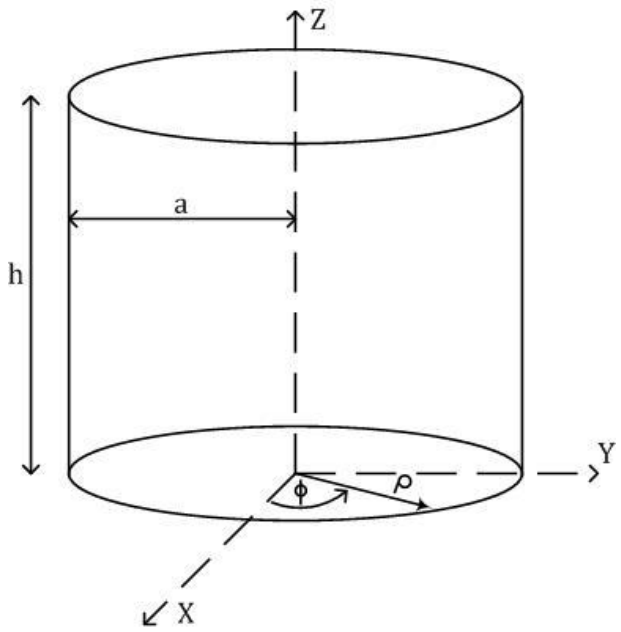

Figure 2.1: Cylindrical Coordinate System.

The general solution to the wave equations for a source-free and lossless media is of the form:[18]

$$\mathbb{E}(\rho,\phi,z) = E_\rho(\rho,\phi,z)\hat{\rho} + E_\phi(\rho,\phi,z)\hat{\phi} + E_z(\rho,\phi,z)\hat{z}, \tag{2.6a}$$

$$\mathbb{H}(\rho,\phi,z) = H_\rho(\rho,\phi,z)\hat{\rho} + H_\phi(\rho,\phi,z)\hat{\phi} + H_z(\rho,\phi,z)\hat{z}. \tag{2.6b}$$

For a TM^z cylindrical coordinate system, the electric field components are defined as

$$E_\rho = -j\frac{1}{\omega\,\mu\,\varepsilon}\frac{\partial^2 A_z}{\partial\rho\,\partial z}, \tag{2.7a}$$

$$E_\phi = -j\frac{1}{\omega\,\mu\,\varepsilon}\frac{1}{\rho}\frac{\partial^2 A_z}{\partial\phi\,\partial z}, \tag{2.7b}$$

$$E_z = -j\frac{1}{\omega\,\mu\,\varepsilon}\left(\frac{\partial^2}{\partial z^2} + \beta^2\right)A_z, \tag{2.7c}$$

and the magnetic field components are defined as[18]

$$H_\rho = \frac{1}{\mu\,\rho}\frac{\partial A_z}{\partial\phi}, \tag{2.8a}$$

$$H_\phi = -\frac{1}{\mu}\frac{\partial A_z}{\partial\rho}, \tag{2.8b}$$

$$H_z = 0. \tag{2.8c}$$

A complete derivation of the field components can be found in *Advanced Engineering Electromagnetics* by Balanis. The variable A_z is the magnetic vector potential in the z-direction and will be discussed further in the next section.

2.1.2 TM Resonant Modes in a Cylindrical Cavity

To simplify the process in obtaining solutions to the electric and magnetic fields, the magnetic vector potential, $\mathbb{A}$, and the electric vector potential, $\mathbb{F}$, are used.

The vector potentials are defined as follows for a cylindrical resonant cavity:[18]

$$\mathbb{A} = A_z(\rho, \phi, z)\hat{z}, \tag{2.9a}$$

$$\mathbb{F} = 0. \tag{2.9b}$$

The vector potential, $\mathbb{A}$, must satisfy the vector wave equation

$$\nabla^2 A_z(\rho, \phi, z) + \beta^2 A_z(\rho, \phi, z) = 0. \tag{2.10}$$

Expanding the equation using cylindrical coordinates results in the following[18]

$$\frac{\partial^2 A_z}{\partial \rho^2} + \frac{1}{\rho}\frac{\partial A_z}{\partial \rho} + \frac{1}{\rho^2}\frac{\partial^2 A_z}{\partial \phi^2} + \frac{\partial^2 A_z}{\partial z^2} + \beta^2 A_z = 0. \tag{2.11}$$

With the details left out for simplicity, the solution to Equation 2.11 for the given cylindrical cavity geometry is[18]

$$\begin{aligned} A_z(\rho, \phi, z) = &\left[A_1 J_m(\beta_\rho \rho) + B_1 Y_m(\beta_\rho \rho)\right] \\ &\times \left[C_2 \cos(m\phi) + D_2 \sin(m\phi)\right]\left[A_3 e^{-j\beta_z z} + B_3 e^{j\beta_z z}\right] \end{aligned} \tag{2.12}$$

$$m = 0, 1, 2, 3 \ldots$$

where the phase constant here is broken into separate components and is defined as

$$\beta^2 = \beta_\rho^2 + \beta_z^2. \tag{2.13}$$

The components that need to be solved for are β_ρ and β_z. These unknowns will be determined by analyzing two of the electric field components.

To simplify this general solution, we note that B_1 must be zero because the fields must be finite everywhere and Y_m is infinite at ρ equal to zero.[18] The solution reduces further by only considering waves that propagate in the z-direction. Two forms of the same solution are[18]

$$A_z(\rho,\phi,z) = B_{mn}J_m(\beta_\rho\rho)\, e^{-j\beta_z z}\,[C_2\cos(m\phi) + D_2\sin(m\phi)]$$
$$= B_{mn}J_m(\beta_\rho\rho)\,[C_2\cos(m\phi) + D_2\sin(m\phi)]$$
$$\times\,[C_3\cos(\beta_z z) + D_3\sin(\beta_z z)] \tag{2.14}$$

Substituting the general simplified equation for $A_z(\rho,\phi,z)$ into Equation 2.7c yields a new equation for E_z.[18]

$$E_z = -j\frac{1}{\omega\,\mu\,\varepsilon}\left(\frac{\partial^2}{\partial z^2} + \beta^2\right)A_z,$$

$$E_z = -jB_{mn}\frac{\beta_\rho^2}{\omega\,\mu\,\varepsilon}J_m(\beta_\rho\rho)\, e^{-j\beta_z z}\,[C_2\cos(m\phi) + D_2\sin(m\phi)]. \tag{2.15}$$

Applying the boundary condition that E_z is zero at ρ equal to a yields[18]

$$E_z(\rho = a,\phi,z) = -jB_{mn}\frac{\beta_\rho^2}{\omega\mu\varepsilon}J_m(\beta_\rho a)\, e^{-j\beta_z z}\,[C_2\cos(m\phi) + D_2\sin(m\phi)] = 0. \tag{2.16}$$

This is only satisfied if $J_m(\beta_\rho a)$ is equal to zero, i.e,

$$J_m(\beta_\rho a) = 0 \Rightarrow \beta_\rho a = \chi_{mn}. \tag{2.17}$$

Rearranging for β_ρ provides the equation defining the first unknown in terms of the cavity radius and χ_{mn} [18]

$$\beta_\rho = \frac{\chi_{mn}}{a} \tag{2.18}$$

$$m = 0, 1, 2, 3 \ldots$$

The *n*th zero of the Bessel function J_m of the first kind of order m is χ_{mn}. The values for χ_{mn} are tabulated for different modes.

Next, using the equation for the electric field component E_ϕ and substituting the general simplified equation for $A_z(\rho,\phi,z)$, provides the equation for E_ϕ in terms of β_z.

$$E_\phi = -j\frac{1}{\omega\mu\varepsilon}\frac{1}{\rho}\frac{\partial^2 A_z}{\partial\phi\,\partial z} \tag{2.7b}$$

$$\begin{aligned} E_\phi = -jB_{mnp}\frac{m\beta_z}{\omega\mu\varepsilon}\frac{1}{\rho}J_m(\beta_\rho\rho)[-C_2\sin(m\phi) + D_2\cos(m\phi)] \\ \times [-C_3\sin(\beta_z z) + D_3\cos(\beta_z z)] \end{aligned} \tag{2.19}$$

The remaining constants can be determined by applying the boundary conditions at the top and bottom of the cavity. These two boundary conditions are

$$E_\phi(0 \le \rho \le a, 0 \le \phi \le 2\pi, z = 0, h) = 0. \tag{2.20}$$

Applying the first boundary condition tells us that D_3 must be equal to zero.[18]

$$\begin{aligned} -jB_{mnp}\frac{m\beta_z}{\omega\mu\varepsilon}\frac{1}{\rho}J_m(\beta_\rho\rho)[-C_2\sin(m\phi) + D_2\cos(m\phi)] \times [-C_3(0) + D_3(1)] = 0 \\ \rightarrow D_3 = 0 \end{aligned} \tag{2.21}$$

Applying the second boundary condition gives the solution for β_z.[18]

$$-jB_{mnp}\frac{m\beta_z}{\omega\mu\varepsilon}\frac{1}{\rho}J_m(\beta_\rho\rho)[-C_2\sin(m\phi) + D_2\cos(m\phi)] \times [-C_3\sin(\beta_z h)] = 0 \tag{2.22}$$

For this to hold, $\sin(\beta_z h)$ must be equal to zero, i.e.,

$$\sin(\beta_z h) = 0 \Rightarrow \beta_z h = \sin^{-1} 0 \;\Rightarrow \beta_z h = p\pi. \tag{2.23}$$

Rearranging for β_z provides the equation defining the second unknown.[18]

$$\beta_z = \frac{p\pi}{h} \tag{2.24}$$

$$p = 0,1,2,3 \ldots$$

With the equations for β_ρ and β_z, the resonant frequency of the cylindrical cavity can be determined using Equation 2.26.[18]

$$\beta^2 = \beta_\rho^2 + \beta_z^2 = \left(\frac{\chi_{mn}}{a}\right)^2 + \left(\frac{p\pi}{h}\right)^2 \tag{2.25}$$

$$(f)_{mnp}^{\mathrm{TM}^z} = \frac{1}{2\pi\sqrt{\mu\varepsilon}}\sqrt{\left(\frac{\chi_{mn}}{a}\right)^2 + \left(\frac{p\pi}{h}\right)^2} \tag{2.26}$$

$$m = 0,1,2,3 \ldots \quad n = 1,2,3 \ldots \quad p = 0,1,2,3 \ldots$$

For a resonant frequency of 30 GHz, the radius to height ratio of the cylindrical cavity for the TM_{011}^z mode can be found using the following equation.[18] In the reverse scenario, for a particular cylindrical cavity, the resonant frequency could be determined.

$$(f)_{011}^{\mathrm{TM}^z} = 30\ \mathrm{GHz} = \frac{1}{2\pi\sqrt{\mu\varepsilon}}\sqrt{\left(\frac{\chi_{01}}{a}\right)^2 + \left(\frac{\pi}{h}\right)^2} \tag{2.27}$$

For the TM_{011}^z, χ_{01} is equal to 2.4049, μ is the relative permeability of the gas, and ε is the relative permittivity of the gas.

Using the boundary conditions and Equation 2.14 applied to all of the electric and magnetic field components in the TM_{011}^z mode, the equations governing the fields in the MET can be derived.[18]

$$E_\rho = j\frac{\mathrm{B}_{011}}{\omega\mu\varepsilon}\frac{\pi}{a}\frac{\chi_{01}}{h}J_0'\left(\frac{\chi_{01}}{a}\rho\right)\sin\left(\frac{\pi}{h}z\right) \tag{2.28a}$$

$$E_\phi = 0 \tag{2.28b}$$

$$E_z = -j\frac{B_{011}}{\omega\mu\varepsilon}\left(\frac{\chi_{01}}{a}\right)^2 J_0\left(\frac{\chi_{01}}{a}\rho\right)\cos\left(\frac{\pi}{h}z\right) \tag{2.28c}$$

$$H_\rho = 0 \tag{2.29a}$$

$$H_\phi = -\frac{B_{011}}{\mu}\frac{\chi_{01}}{a}J_0'\left(\frac{\chi_{01}}{a}\rho\right)\cos\left(\frac{\pi\, z}{h}\right) \tag{2.29b}$$

$$H_z = 0 \tag{2.29c}$$

2.1.3 Transmission Line Theory

Understanding the power transfer from the microwave source and the MET is essential for optimizing the performance of the thruster. There are three main types of transmission lines.[19] The first and oldest form of transmission line is the waveguide. The waveguide handles high powers with low loss but they tend to be more expensive and larger in size. The second type of transmission line is the coaxial line. Coaxial lines are less expensive and more compact than waveguides, but it can be difficult to fabricate the necessary microwave components. The final type of transmission line is planar transmission lines. These are the most commonly used transmission line because they are compact, inexpensive, and can be easily integrated into microwave circuits.

A transmission line is characterized by a propagation constant, a characteristic impedance, and, if the line is lossy, attenuation. The propagation constant, β, for the TM_{011}^{z} mode was derived in the previous section. The characteristic impedance of a line, Z_0, is determined by the ratio of voltage to current for the traveling wave on the line.[19] The attenuation, α, is the rate of decay of a signal and should be minimized.

Transmission line propagation is broken up into transverse electromagnetic (TEM), transverse electric (TE), and transverse magnetic (TM) wave propagation. TEM waves can exist if the transmission line has two or more conductors while TE and TM waves can exist on transmission lines with a single conductor.

The network consisting of the MET and the coaxial microwave transmission lines can be modeled as a lossless transmission line (coaxial line) terminated with a load impedance, Z_L, which represents the MET.

Figure 2.2: Modeled Lossless Transmission Line Network of the MET.

Matching the load impedance to the characteristic impedance of the line is important for optimal performance of the MET. A well matched load and line impedance minimizes power reflections and allows for maximum power transfer from the line to the load. When a line and load are mismatched, part of the incident traveling wave is reflected. The wave amplitude of the reflected voltage normalized to the wave amplitude of the incident voltage is known as the voltage reflection coefficient, Γ,[19]

$$\Gamma = \frac{Z_L - Z_0}{Z_L + Z_0}. \tag{2.30}$$

When Γ is equal to zero, there is no reflected wave. For this to occur, Z_L must be equal to Z_0. The voltage and current on a transmission line is the superposition of an incident and reflected wave.[19] This type of wave is called a standing wave. The incident and reflected power on a line can be expressed as the following: [19]

$$P_{\text{inc}} = \frac{1}{2}\frac{\left|V_{0,\text{inc}}\right|^2}{Z_0}, \tag{2.31}$$

$$P_{\text{ref}} = \frac{1}{2}\frac{\left|V_{0,\text{inc}}\right|^2}{Z_0}|\Gamma^2|. \tag{2.32}$$

The average power on the line is equal to the incident power minus the reflected power:[19]

$$P_{\text{ave}} = \frac{1}{2}\frac{\left|V_{0,\text{inc}}\right|^2}{Z_0}(1 - |\Gamma^2|). \tag{2.33}$$

From Equation 2.33 it can be seen that the average power on the line is related to the characteristic impedance of the line and the reflection coefficient. When the load is not

matched to the line, not all of the power is delivered to the load. To describe the power loss associated with the mismatch, the *return loss* is used[19]

$$\mathrm{RL} = -20\log|\Gamma|. \tag{2.34}$$

2.2 Plasma Theory

2.2.1 Criteria of a Plasma

As previously discussed, the MET heats the propellant by means of a plasma. As such, the understanding of plasmas is also important to the operation and design of the MET. Plasmas are a complex state of matter; therefore, only a brief overview of their nature will be discussed in this section.

A plasma is defined by Chen in an *Introduction to Plasma Physics and Controlled Fusion* as a quasineutral gas consisting of neutral and charged particles.[20] The local concentrations of positive and negative areas generate an electric field. The electric fields induce current flow, which in turn creates magnetic fields. Particles anywhere in the plasma are affected by the motion of other charged particles due to the electric and magnetic fields they create. Common forms of plasmas are lightning bolts, neon signs, the aurora borealis lights, Van Allen radiation belts, and the solar wind. A fundamental characteristic of a plasma is its ability to shield out electric potentials.[20] The Debye length, λ_D, is a measure of the shielding thickness of the plasma. This leads to the first criteria that must be satisfied for an ionized gas to be considered a plasma.[20]

$$\lambda_D \ll L \tag{2.35}$$

In order for the Debye shield to be possible, there must be a sufficient number of particles, N_D, in the charged gas. The second criteria for an ionized gas to be considered a plasma requires[20]

$$N_D \gg 1. \tag{2.36}$$

The final criterion that must be met is related to the frequency of collisions with neutral atoms in the plasma, ω_c, and the mean time between collisions, τ_c. In order for the motion of the charged cloud to be controlled by electromagnetic forces, the following must be met[20]

$$\omega_c \tau_c > 1. \tag{2.37}$$

2.2.2 Plasma Formation and Dissipation

In general, plasma formation occurs by gas breakdown. With a strong enough electric field, electrons can be stripped from molecules resulting in two oppositely charged particles, an ion and an electron. In the MET, gaseous breakdown is designed to occur in the center of the cavity and near the nozzle entrance by concentrating the electric field at that location, as discussed previously. The forces felt by the electrons and ions follow the Lorentz Law,

$$\mathbb{F} = q\mathbb{E}. \tag{2.38}$$

This equation shows how the charge of the particle determines the direction of the force felt by the particle. Electrons and ions are pulled in opposite directions. When the rate of electron removal from neutral particles is greater than the rate of electron recombination, gaseous breakdown occurs and forms a plasma. To sustain a plasma, ionization must continue to occur at a rate faster than diffusion and recombination combined.

Continuous ionization is maintained primarily through inelastic collisions between electrons and neutral particles. A collision is considered to be inelastic when kinetic energy is not conserved.[2] However, momentum is conserved such that the collision results in the neutral atom becoming excited or, with sufficient kinetic energy, fully ionized.[2]

Plasmas have a density gradient, which makes the plasma diffuse toward lower concentrations. The lower density regions in the MET are near the walls where the density is zero. Recombination occurs when an ion and low velocity electron collide and form a neutral atom. In order to conserve momentum a third body must be present. The process is

referred to as radiative recombination when the third body is an emitted photon.[2] If the third body is a particle, the process is called three-body recombination.[2] The rate of diffusion and recombination can be minimized with a magnetic field.

CHAPTER 3

THRUSTER DESIGN

3.1 Design Objectives

The primary objectives for the design of the 30-GHz MET are that it operates in the TM_{011}^{z} mode and the dimensions are such that the resonant frequency is 30 GHz. The previous generations of thrusters have shown that the TM_{011}^{z} mode is ideal for producing a free-floating plasma located near the nozzle entrance. This location for the plasma allows for the maximum thermal energy transfer to the propellant. The resonant frequency of 30 GHz is well suited for the physical size requirements of the thruster. Frequencies around 30 GHz yield thruster dimensions, input power requirements, and total system mass that are ideal for use on a CubeSat.

The secondary considerations for the design of the thruster are the input power, pressure sealing capabilities, propellant input location, and the ability to visually confirm that a plasma has formed during experimentation. An input power of up to 10 W is the expected power needed to generate and maintain a plasma. For the initial testing of the thruster, a vacuum cap will be attached to the end of the nozzle to allow the thruster to exhaust to simulated vacuum conditions. In order to achieve the vacuum, the thruster must be sealed well enough such that it can sustain a pressure below 25 Torr. Through previous experiments, this is the minimum pressure needed to generate a plasma. In order to know that the partial vacuum has been achieved, a pressure transducer port needs to be designed into the thruster geometry. Previous Penn State MET thrusters have utilized a variety of propellants. The limiting factor in this thruster will be the physical size constraints of the propellant feed. Finally, for experimental purposes, a visual confirmation that the plasma has been lit would be ideal. Prior MET's have used machined-in windows, but the size of this thruster does not lend itself to the use of the same type of window.

3.2 Key Features of Predecessors

In order to understand the design choices made for the 30-GHz MET, it is essential to look at how the earlier MET's were designed. The first MET was designed to operate at a frequency of 2.45 GHz. The cavity was broken into two sections by a dielectric plate, known as a pressure plate.[8] The pressure plate maintained a high enough pressure near the bottom of the cavity to prevent the plasma from forming there. Instead the plasma was forced to form near the nozzle entrance.[8] The physical properties of the dielectric effectively made it transparent to the microwave energy.[8] There were three propellant injectors entering on the top half of the cavity that angled upwards toward the nozzle.[8] A viewing window was on one side of the top half of the thruster cavity.[8] The cavity diameter was 10.16 cm, the height was 15.87 cm, and the bottom half of the cavity had an adjustable shorting plate for continuous tuning capability.[8]

The next thruster operated at 7.5 GHz with many of the same design characteristics as the 2.45-GHz MET but with a few improvements. The shape of the exterior of the 7.5-GHz thruster resembled a cube whereas the outer walls of its predecessor formed a cylinder. This allowed for easier connections to the cavity. In addition, the propellant injectors were moved closer the nozzle entrance and inserted tangentially to the cavity. The cavity diameter was 3.8 cm, the height was 5.08 cm, but unlike the 2.45-GHz thruster, the new design did not consist of an adjustable shorting plate.[9] The 14.5-GHz thruster, also known as the "miniMET", had a design that was very similar to the 7.5-GHz MET. The miniMET cavity was also physically sized down.

3.3 Thruster Design Overview

The first stage in the design of the thruster is to specify the thruster's dimensions. The cavity dimensions must be chosen such that they induce a plasma near the nozzle entrance, as previously discussed. To obtain the dimensions, Equation 2.27 was used. Any geometric disturbances in the cavity walls, such as the pressure port and propellant inlet, and the introduction of the propellant flow perturb the resonant frequency. These disturbances affect the permittivity of the cavity medium, reducing the resonant frequency. The

theoretical resonant frequency determined based on Equation 2.27 should be close enough to the actual resonant frequency to be used interchangeably. As previously discussed, there are an infinite number of height-to-radius ratios available. The ratio determines the field configuration at the cavity's mid-plane. A higher height-to-radius ratio results in a lower concentration of the electric field at the mid-plane. The desired outcome is to have the maximum electric field strength at the ends of the cylinder. A ratio of 3.5 has been selected for the 30-GHz thruster based on the performance of prior MET designs. Inserting the ratio and known constants into Equation 2.27 results in a cavity radius of 0.41 cm. Using the radius and the ratio of 3.5, the height of the cavity is determined to be about 1.43 cm.

$$30\text{ GHz} = \frac{1}{2\pi\sqrt{\mu\,\varepsilon}}\sqrt{\left(\frac{2.4049}{a}\right)^2 + \left(\frac{\pi}{3.5\,a}\right)^2} \rightarrow a = 0.40857\text{ cm}$$

$$\frac{h}{a} = 3.5 \rightarrow h = 1.4299\text{ cm}$$

With the height, h, and radius, a, of the cavity determined, the method of propellant input is considered. Instead of multiple injectors, a single propellant line will be inserted near the nozzle entrance of the thruster. Due to the small size of the thruster, it is expected that one propellant line will be sufficient; however, the cavity will be designed to allow for a second propellant input should it be needed.

The nozzle plate, along with the rest of the cavity, is made out of 6061 aluminum. The nozzle has an entrance diameter of 0.0059 inches and an exit diameter of 0.0087 inches. These dimensions were chosen based on the drilling depth attainable with a 0.0059 inch drill. It would be more ideal to have a single diameter through the entire nozzle plate but manufacturing constraints necessitated a transition to 0.0087 inches for the exit diameter. A Parker O-ring groove size 2-013 is used to seal the nozzle plate to the cavity body.

The microwave power enters the cavity through an antenna that is inserted through the bottom of the cavity. Another Parker O-ring groove size 2-013 is used to seal the bottom plate to the cavity body. The ideal antenna for the 30-GHz MET should create a strong electric field near the entrance to the nozzle. The antenna for the thruster was chosen based on the results of the electromagnetic modeling of the cavity and antenna options.

3.4 Electromagnetic Modeling

Over the past decade, computational modeling has played a larger role in the design of the MET. Experimental research can be an expensive way to analyze the behavior of the MET and in some cases may be too time intensive. Electromagnetic modeling of the resonant cavity decreases the time and money needed to analyze the physics and the cavity environment.

Electromagnetic modeling of the 30-GHz thruster with the pre-determined dimensions from Chapter 2 will provide three key aspects to the thruster design. The first set of models will be used to determine the optimal antenna size for the cavity. The electric field strength near the nozzle entrance will be compared for an SMA antenna, an SSMA antenna, and a 2.4-mm antenna. The second set of models will provide insight into the effects of antenna length. An antenna that is flush (zero length), 0.5 mm long, and 1 mm long will be examined to see the effects of imperfect antenna sizing on the resonant frequency and electric field strength. Due to the small size of the cavity, expected machining inaccuracies of up to 0.2 mm will be examined by creating models of the cavity with varying radii. This set of models will determine how variations in cavity radius affect the resonant frequency of the cavity.

COMSOL Multiphysics software was used to perform all of the 3D, RF modeling of the thruster. The first step of modeling the thruster is to either import the geometry from another program such as SolidWorks or create it with the COMSOL interface. For these models, the geometry was created using the COMSOL interface. A completed schematic of the geometry for the cavity with an antenna length of one millimeter is shown in Figure 3.1.

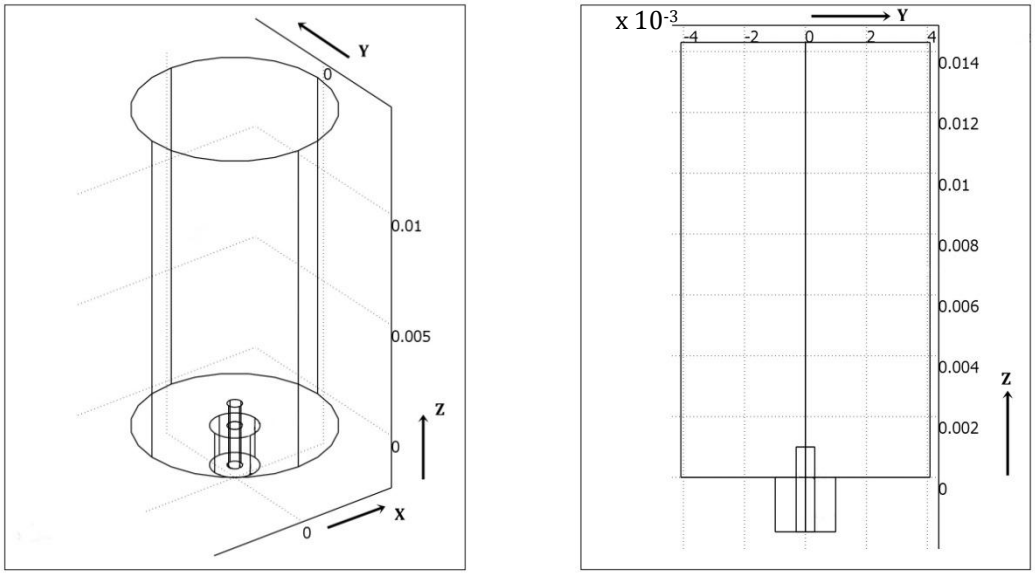

Figure 3.1: Geometry Setup for a 1 mm Antenna Length.

To determine the resonant frequency, a frequency analysis should be performed on the model. This was done by analyzing the electric field strength inside of the cavity for a range of frequencies. The boundary conditions allow for inputs and outputs to be designated along with the type of boundary along the walls of the cavity.

The boundary condition for each face of the cavity was set as perfect electric conductor except the bottom of the antenna. The bottom of the antenna was set as a coaxial port with wave excitation with 10 W input power as shown in Figure 3.2. The microwave energy is introduced into the cavity via the antenna and thus the designation of that face as a port.

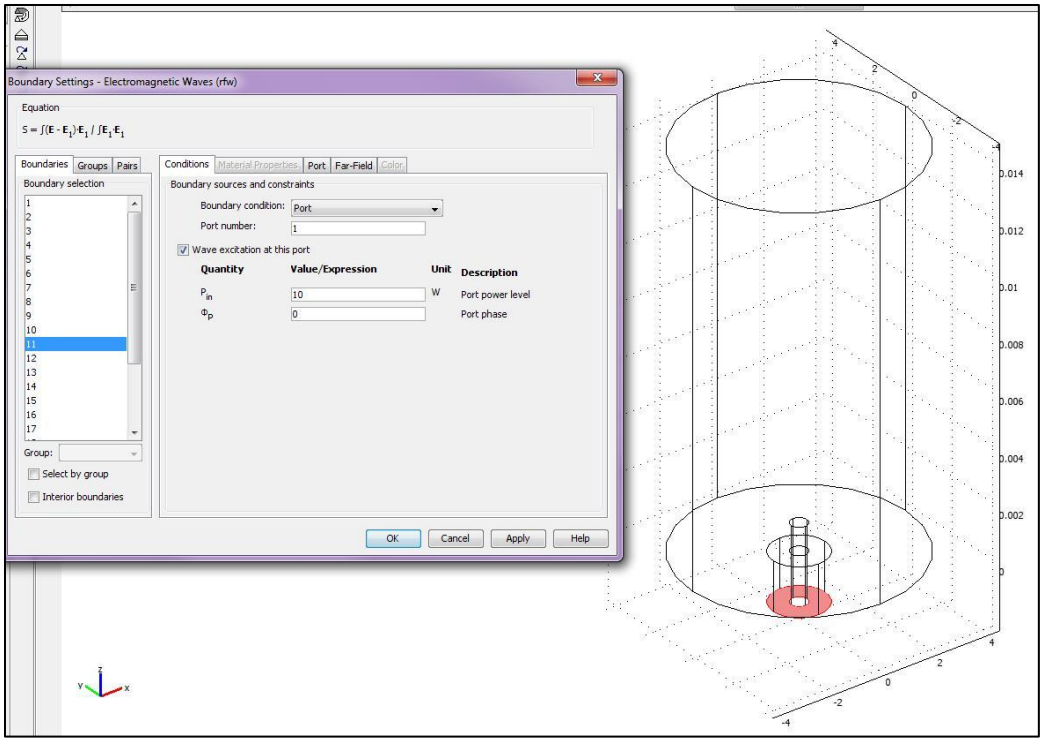

Figure 3.2: Boundary Condition Specified for the Antenna.

The next task is to designate the subdomain settings that allocate the domain material and its properties. Multiple materials are available from the COMSOL library or custom material properties can be specified. From the library of materials, the insulator around the antenna was set to PTFE (Teflon) and the rest of the cavity was set to air. A coarse mesh was used and is shown in Figure 3.3. A finer mesh would provide higher precision but is more computationally expensive.

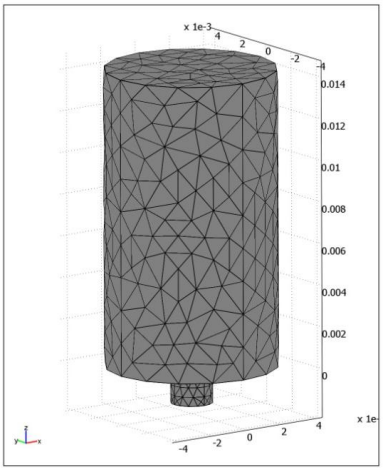

Figure 3.3: Mesh for the 1 mm Antenna Length Model.

Using the *Solver Parameters* control box shown in Figure 3.4, the solver was set to perform a parametric sweep from 29 GHz to 31 GHz.

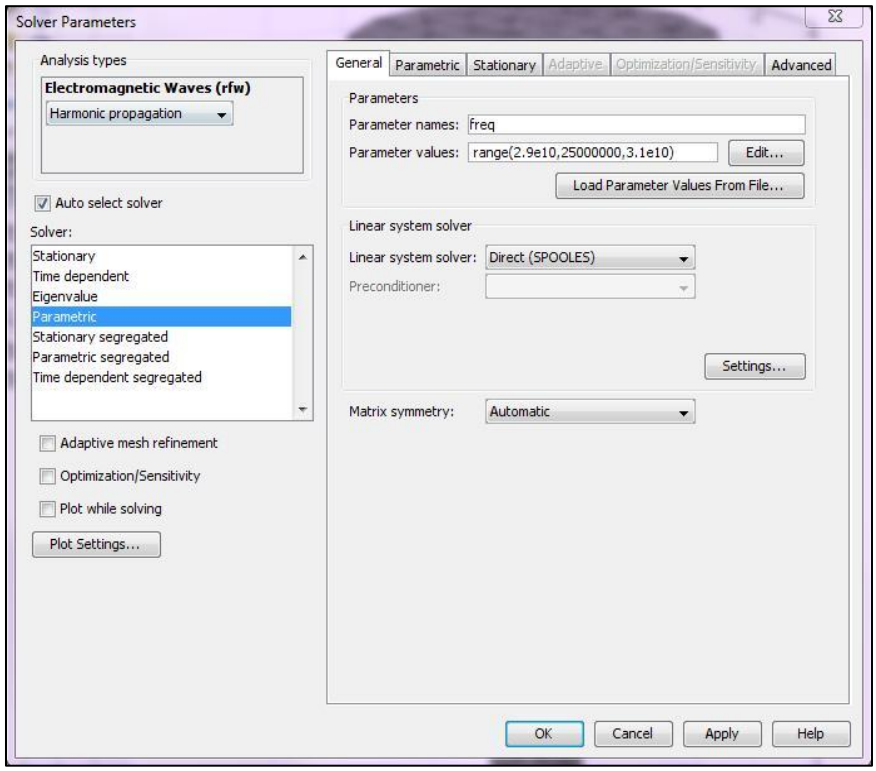

Figure 3.4: Solver Parameters for the Frequency Span.

CHAPTER 4

COMPUTATIONAL RESULTS AND DISCUSSION

COMSOL Multiphysics software was used to model the electromagnetic behavior inside of the MET cavity. The modeling was performed in order to provide insight into three design considerations for the 30-GHz MET. First, an antenna must be chosen that provides excellent microwave power coupling to the cavity. The maximum power transfer to the cavity is dependent on the dimensions of the antenna. Each of the antenna options for the thruster was modeled in COMSOL. The electric field intensity near the nozzle entrance and the resonant frequency of the cavity were analyzed for each of the antennas. Second, the length of the antenna can be altered to provide the best power coupling to the cavity. Three different antenna lengths and the thruster cavity were modeled with COMSOL. The electric field intensity near the nozzle entrance and the resonant frequency of the cavity for each of the antenna lengths were of particular interest. Third, due to the small physical size of the thruster and the high accuracy of machining required, it may not be possible to produce the exact thruster diameter modeled in COMSOL. Cavities with slightly larger and slightly smaller diameters were created and analyzed in COMSOL in an effort to understand how cavity diameter affects the electric field strength and resonant frequency.

4.1 Antenna Size Optimization

For maximum power to be transferred to the cavity, an optimal antenna must be selected. The optimal antenna dimensions scale with the physical size of the cavity. Commercial availability of antennas must also be considered. The cavity has a radius of 0.41 cm so there are three antenna sizes that would physically fit. The antennas are designated based on their connection type: SMA, SSMA, and 2.4-mm. Physically, the SMA antenna is the largest and the 2.4-mm antenna is the smallest. The dimensions of the antennas were specified when creating the geometry of the cavity and antenna in COMSOL. In Figure 4.1, a schematic

of the cavity's bottom surface, where the antenna enters the cavity, is shown for each of the antennas. The outer blue circle is the edge of the cavity. The circle with the shading, designated CO1, is the region where the antenna extends down and away from the cavity as shown in Figure 4.2. This part of the antenna was designated as Teflon in the subdomain settings as opposed to the rest of the cavity which was set as air. The inner circle labeled E1 is the antenna that enters the cavity also shown in Figure 4.2.

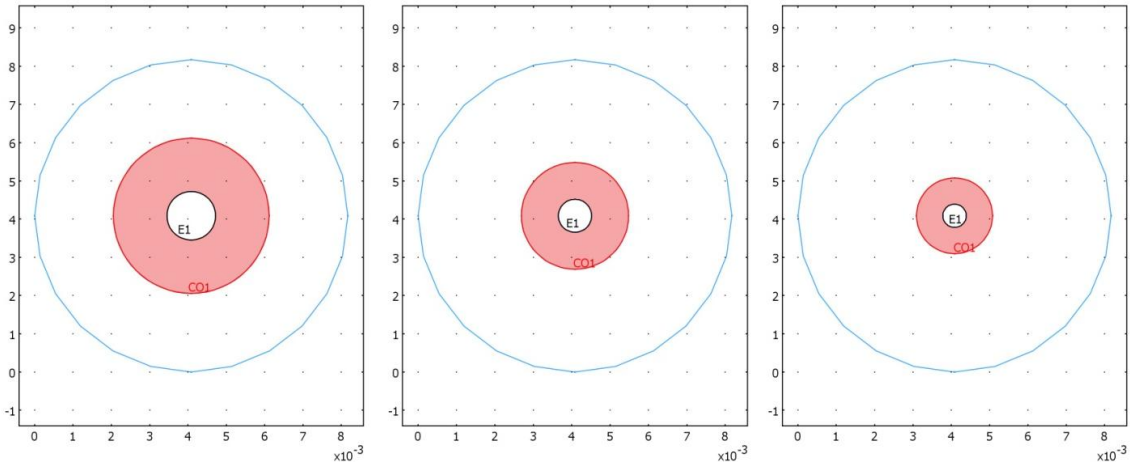

Figure 4.1: Variation of Antenna Diameter for the SMA (left), SSMA (center), and 2.4-mm (right) Antennas in Relation to the Cavity Diameter.

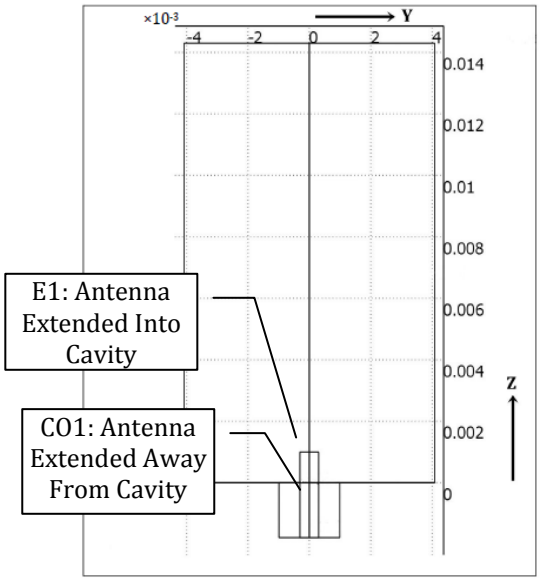

Figure 4.2: Antenna Extensions and Labels in the Cavity Geometry.

For this portion of the COMSOL modeling, the part of the antenna extending into the cavity, E1, was modeled as having zero length (flush with the bottom cavity wall). Previous research on the MET at lower frequencies has shown that maximum energy is transferred to the cavity when the antenna is nearly flush with the bottom of the cavity. The optimal length of the antenna is evaluated in Section 4.2. The part of the antenna extending down and away from the cavity, CO1, was specified as having a length equal to one eighth of the cavity height or about 0.18 cm for all of the COMSOL modeling. This value was chosen based on the typical lengths of the commercial antennas. The antenna geometries for the three simulations are shown in Figure 4.3.

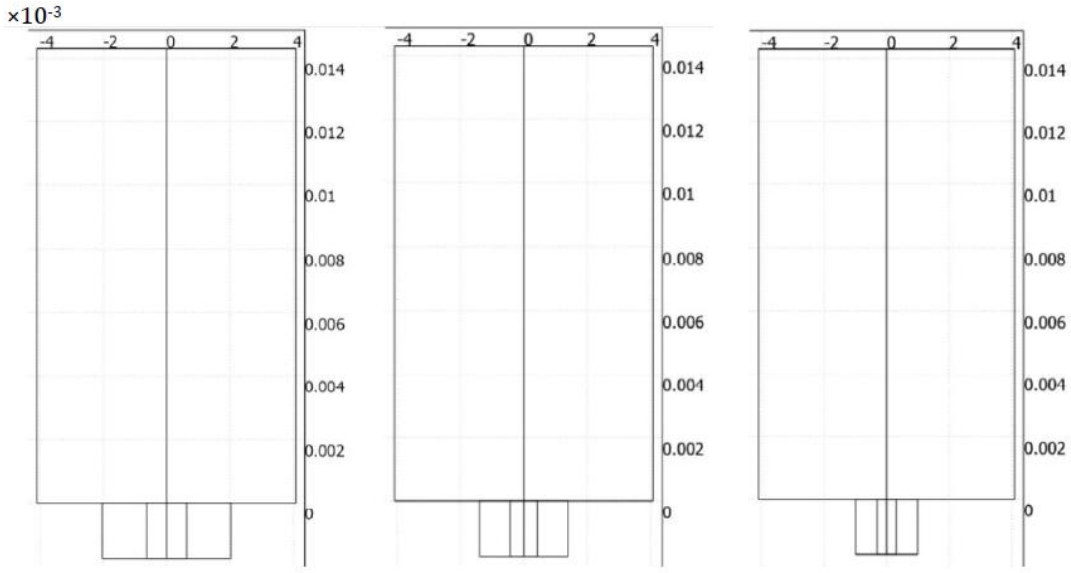

Figure 4.3: Antenna Geometry for SMA (left), SSMA (center), and 2.4-mm (right) Antennas.

The simulations yielded the magnitude and streamlines of the electric field for an input power of 10 W. Figure 4.4 shows both quantities in the *y*–*z* plane at the center of the cavity. The electric field strength scale ranges from zero volts per meter (V/m) to a maximum of 1.5×10^{6} V/m.

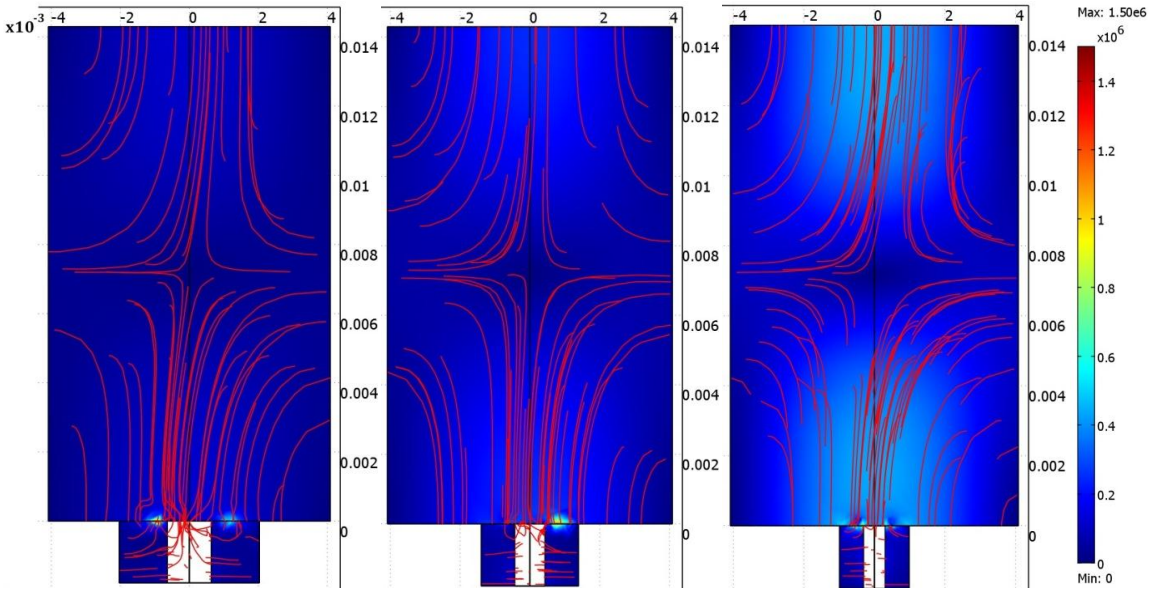

Figure 4.4: Electric Field Magnitude (V/m) Contour Plot and Streamline Plot at 30 GHz for SMA (left), SSMA (center), and 2.4-mm (right).

Figure 4.4 shows that the streamlines for all three cases are similar to one another and exhibit the behavior of the TM_{011}^{z} mode. Based on the larger color gradient shown in the contour plots of the three cases, the 2.4-mm antenna displays higher electric field strength near the top and bottom of the cavity than either the SMA or SSMA geometry.

Another aspect of antenna selection that must be evaluated is the resonant frequency of the cavity for each of the antenna geometries. A line plot of electric field strength versus frequency for an axial point that is 0.014 m from the bottom of the cavity was created for each of the antennas. This point was chosen because it is located at the top of the cavity near the nozzle entrance where the plasma will form. The frequency sweep can be seen in Figure 4.5. The strongest electric field was obtained with the 2.4-mm antenna and it occurred closest to the desired resonant frequency of 30 GHz.

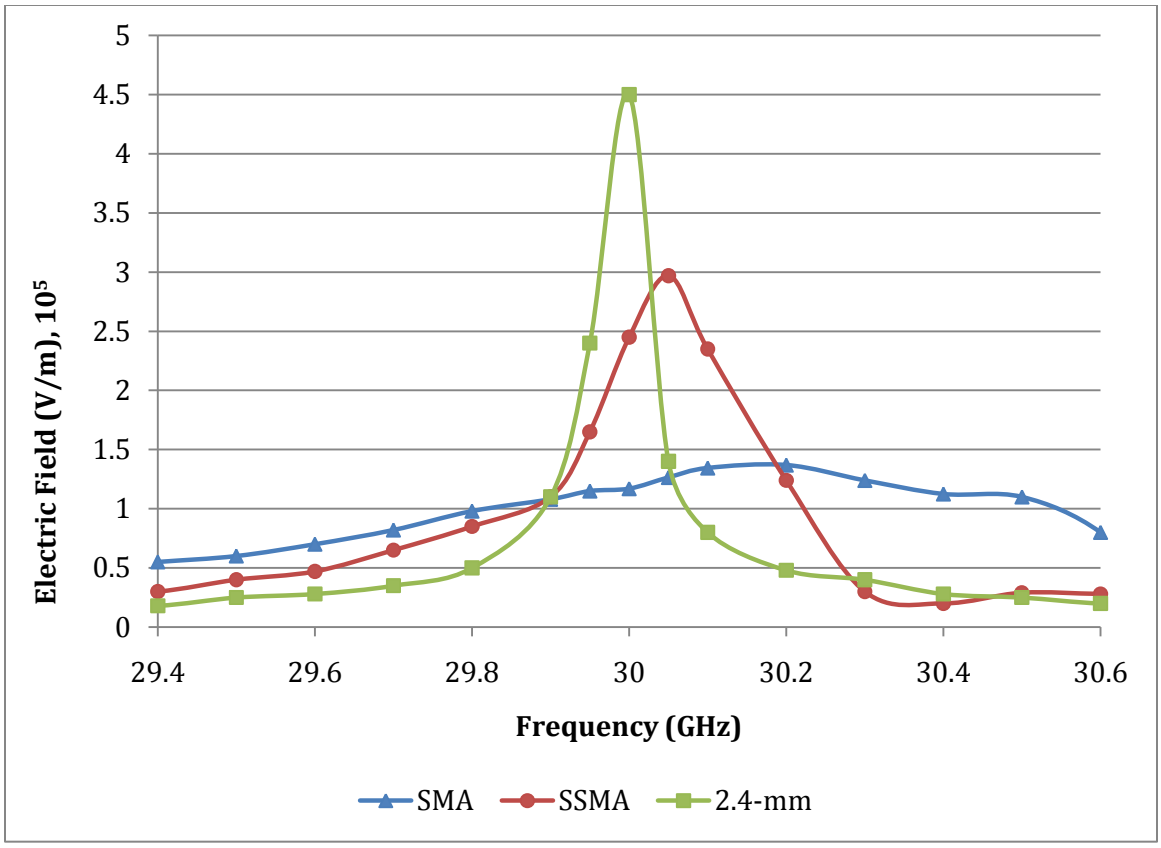

Figure 4.5: Electric Field Strength vs. Frequency for the SMA, SSMA, and 2.4-mm Antennas.

The peak electric field intensity for the SMA antenna was 1.37×10^5 V/m at a frequency of 30.15 GHz. The peak electric field intensity for the SSMA antenna was 3×10^5 V/m at a frequency of 30.05 GHz. The peak electric field intensity for the 2.4-mm antenna was 4.5×10^5 V/m at a frequency of 29.97 GHz. Although the TM^z_{011} mode characteristics were attained in all three simulations, the strongest electric field and the desired resonant frequency were obtained using the 2.4-mm antenna, thus the dimensions of the 2.4-mm antenna is the ideal choice for this cavity.

4.2 Effects of Antenna Length

The length that the antenna protrudes into the cavity affects the resonant frequency of the cavity and the electric field strength. Previous MET research has shown that there is an ideal length for the antenna that provides the highest electric field intensity near the nozzle entrance. The optimal antenna length is specific to the size and shape of the cavity. This is

an excellent example of the benefits of computationally modeling the cavity. Obtaining the optimal length experimentally would require multiple antennas, each cut to a different size which is both time consuming and expensive.

The antenna lengths modeled are 0.0 mm (flush with the bottom cavity wall), 0.5 mm, and 1 mm. Each of the cavity and antenna geometries and their corresponding electric field solutions are shown in Figure 4.6. The figure shows the *y*–*z* plane through the center of the cavity.

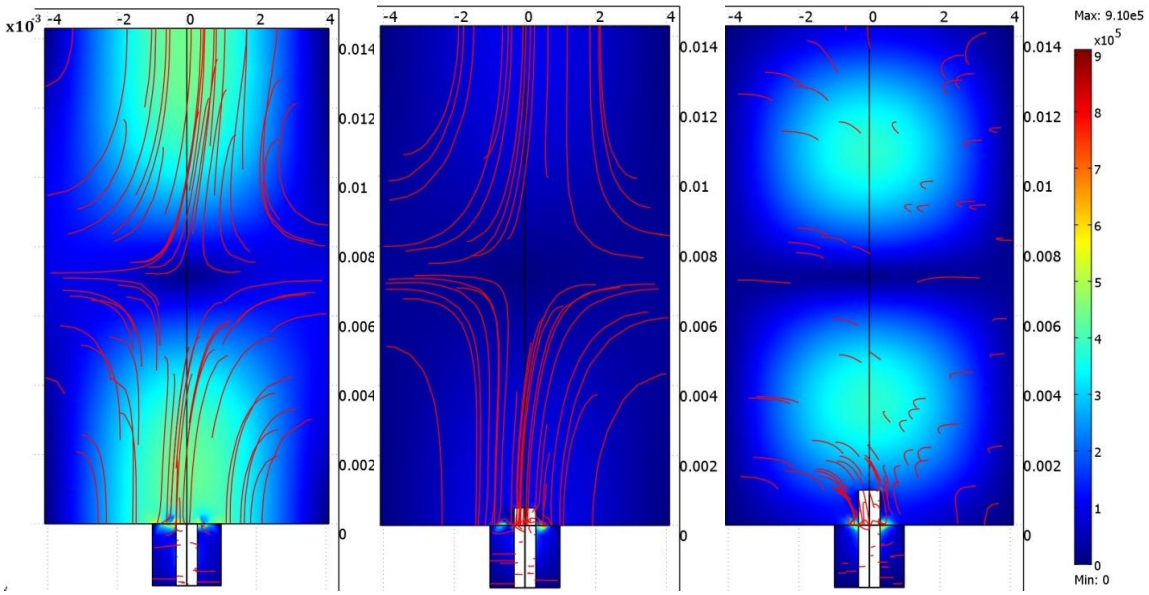

Figure 4.6: Electric Field Magnitude (V/m) Contour Plot and Streamline Plot at 30 GHz for 0.0 mm (left), 0.5 mm (center), and 1 mm (right) Antenna Lengths in the *y*–*z* Direction.

The electric field scale ranges from zero V/m to a maximum of 9.1×10^5 V/m. At first glance, the magnitude and streamlines of the three cases appear to be very different from one another. The electric field streamlines produced by the flush and 0.5-mm antennas still indicate the presence of the TM^z_{011} mode, but the 1-mm antenna streamlines do not. The magnitudes of the electric field are also dissimilar between the three cases. The flush antenna has the electric field that is strongest at the two ends of the cavity, indicated by the lighter color. The 0.5-mm antenna, when compared to the flush antenna, appears to have a much smaller electric field intensity, which is indicated by the lack of gradient. Electric field intensity of the 1-mm antenna appears to be comparable to the flush antenna but the location of the two concentrations has shifted towards the center of the cavity.

Analyzing other planes of the cavity can help to better understand the electric field configuration for each of the antenna geometries. Figure 4.7 shows the electric field magnitude and contour plots of the three cavities in the *x*–*z* plane rather than the *y*–*z* plane. The scale is the same as Figure 4.6 with a maximum of 9.1×10^5 V/m.

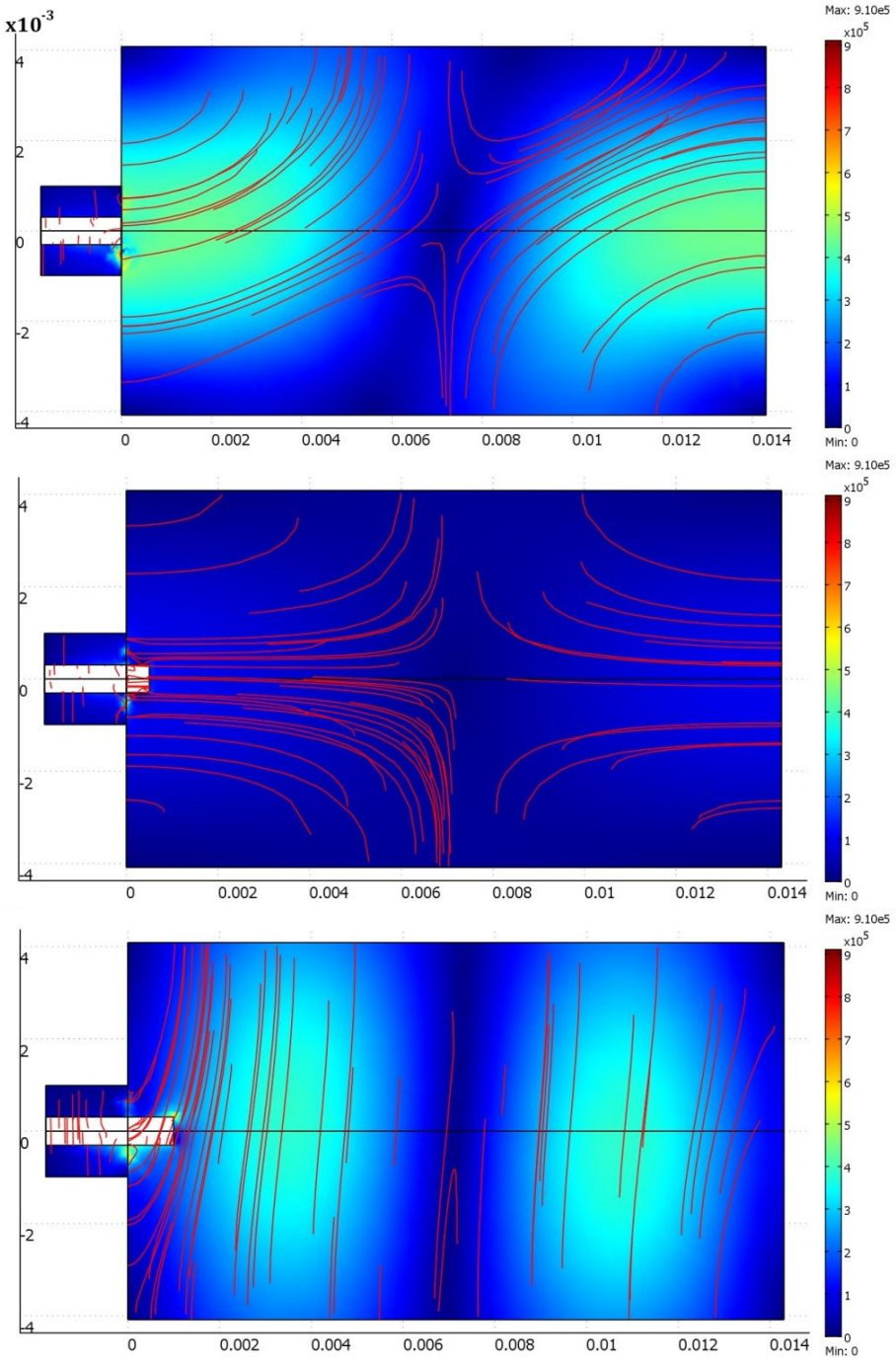

Figure 4.7: Electric Field Magnitude (V/m) and Streamlines at 30 GHz for 0 mm (top), 0.5 mm (middle), and 1 mm (bottom) Antenna Lengths in the *x*–*z* Direction.

This view of the cavity shows the electric field streamlines more clearly. In Figure 4.6, the electric field streamlines for the flush antenna resemble the TM_{011}^{z} mode as shown in Figure 1.5, but in Figure 4.7 the field lines appear slightly distorted. The 0.5-mm streamline configuration in the *x*–*z* plane looks the same as the *y*–*z* plane. However, the streamlines for the 1-mm antenna are severely distorted from the TM_{011}^{z} mode configuration.

Another frequency sweep of the cavities was performed to understand the effects that antenna length has on the resonant frequency and the peak electric field. The same point as in Section 4.1 was chosen, an axial point that is 0.014 m from the top of the cavity.

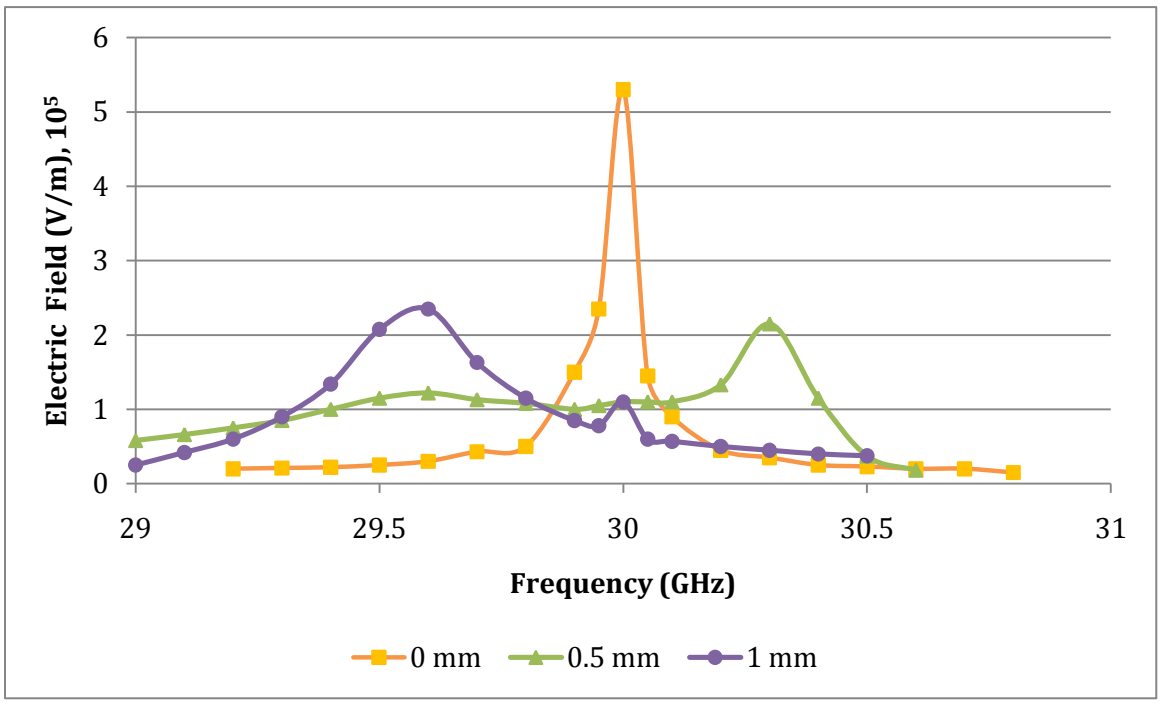

Figure 4.8: Electric Field Strength vs. Frequency for Antenna Lengths 0 mm, 0.5 mm, and 1 mm.

The maximum electric field intensity for the 0-mm antenna was 5.3×10^5 V/m at 29.98 GHz. The maximum electric field intensity for the 0.5-mm antenna was 2.15×10^5 V/m at 30.33 GHz. The maximum electric field intensity for the 1-mm antenna was 2.35×10^5 V/m at 29.57 GHz. The 1-mm antenna also had a spike in electric field strength at 30 GHz, but it was much smaller than the peak at 30 GHz for the 0-mm antenna.

The strongest electric field was created by the antenna length of 0 mm and was obtained at the resonant frequency of interest, 30 GHz. The streamlines for the 0.5-mm antenna showed the closest resemblance to the TM_{011}^{z} mode, whereas the 0-mm antenna's streamlines were slightly distorted. The 1-mm antenna proved to be deficient in terms of resonant frequency, electric field strength, and streamline configuration. Based on this information, it was determined that the flush antenna length will yield the highest electric field strength near the nozzle entrance at 30 GHz. It is possible that an antenna length between 0.0 mm and 0.5 mm would outperform the antenna that was selected. However, the accuracy required to cut the antenna length to the desired length would be difficult.

4.3 Effects of Variations in Cavity Radius

The dimensions of the cavity strongly influence the performance and resonant frequency of the MET. Due to the tight manufacturing tolerances of this thruster, the effects of slight variations in cavity radius were examined. Models were created of the flush 2.4-mm antenna with a cavity radius that is ±0.1 and ±0.2 mm from the exact cavity radius of 4.0857 mm.

The electric field strength and streamlines at 30 GHz along the center *y*–*z* plane of the cavity are shown in Figure 4.9 for the exact radius, +0.1 mm, and +0.2 mm cavities. The scale ranges from 0 V/m to 9.1×10^{5} V/m.

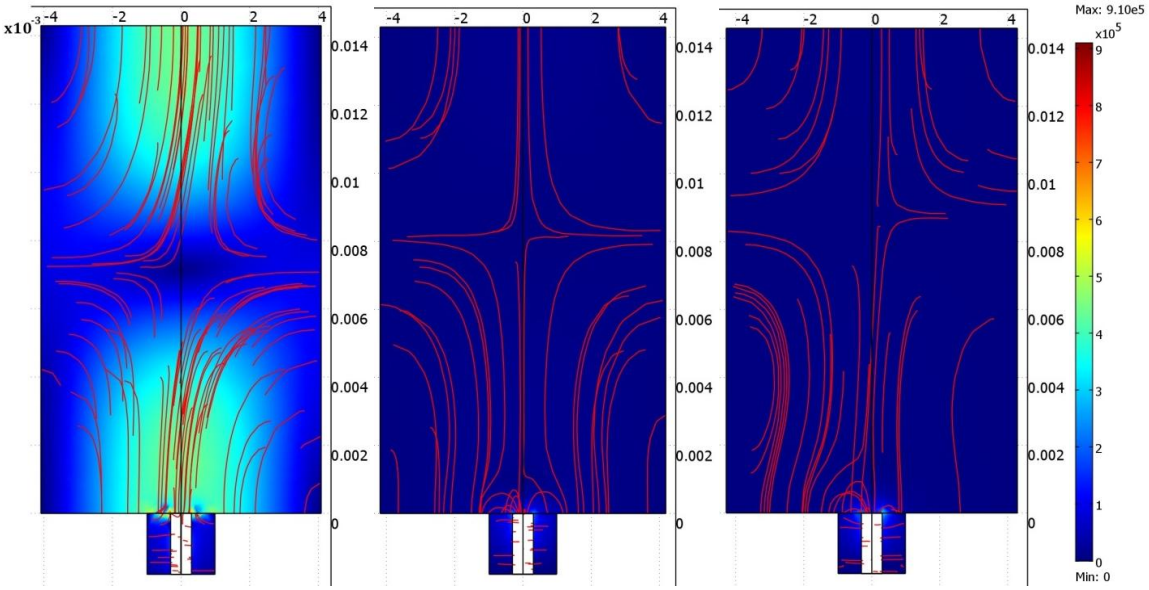

Figure 4.9: Electric Field Strength (V/m) and Streamlines at 30 GHz for the Exact Radius (left), +0.1 mm (center), and +0.2 mm (right).

The streamlines for the +0.1-mm cavity still conform to the TM_{011}^{z} mode, but have effectively shifted towards the top of the cavity, away from the antenna. The +0.2-mm cavity streamlines begin to distort as they approach the bottom of the cavity. Also, by looking at the color gradients, it can be seen that the magnitude of the electric field at the ends of the +0.1-mm and +0.2-mm cavities are significantly lower compared to the exact radius cavity.

COMSOL models were also created for the −0.1-mm and −0.2-mm cases and the results are shown in Figure 4.10. The scale for these plots is the same as Figure 4.9.

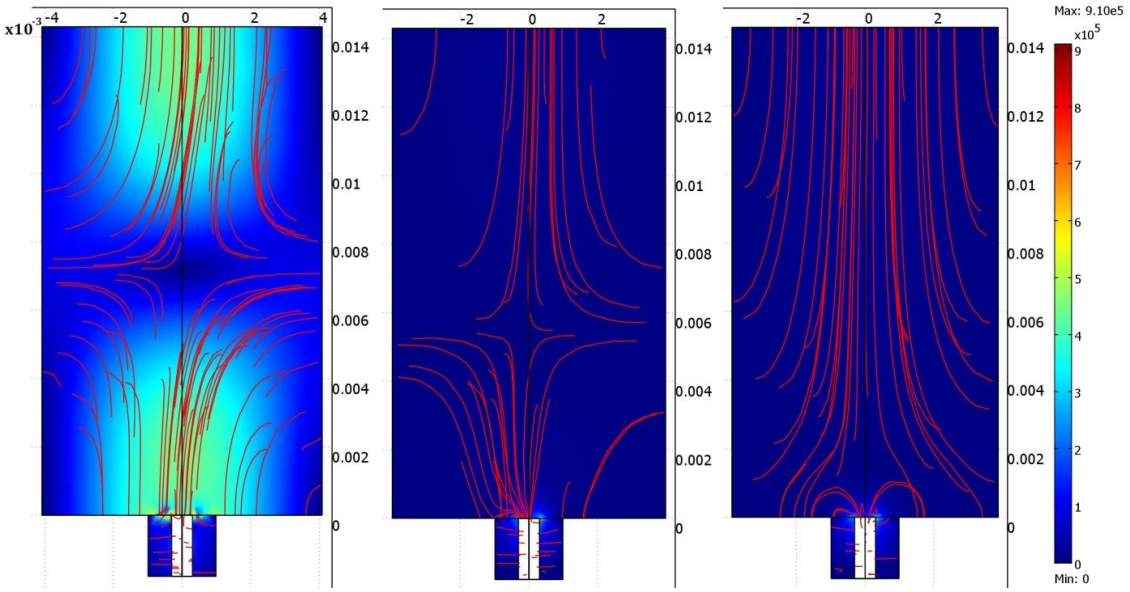

Figure 4.10: Electric Field Strength (V/m) and Streamlines at 30 GHz for the Exact Cavity Dimensions (left), −0.1 mm (center), and −0.2 mm (right).

For the −0.1-mm cavity, the streamlines have effectively shifted closer to the antenna as opposed to the +0.1-mm cavity, where they shifted away from the antenna. For the −0.2-mm cavity, the streamlines are completely distorted from the TM_{011}^{z} mode configuration. The streamlines appear to run the entire length of the cavity instead of diverging outwards at the mid-plane.

A frequency span was performed from 28.5 GHz to 31 GHz for each of the cavity sizes to determine how the resonant frequency of each cavity was affected by the change in radius. The results are shown in Figure 4.11. The frequency span was performed on a single point in the cavity, which is located along the axis of the cavity at a z-distance of 0.014 m.

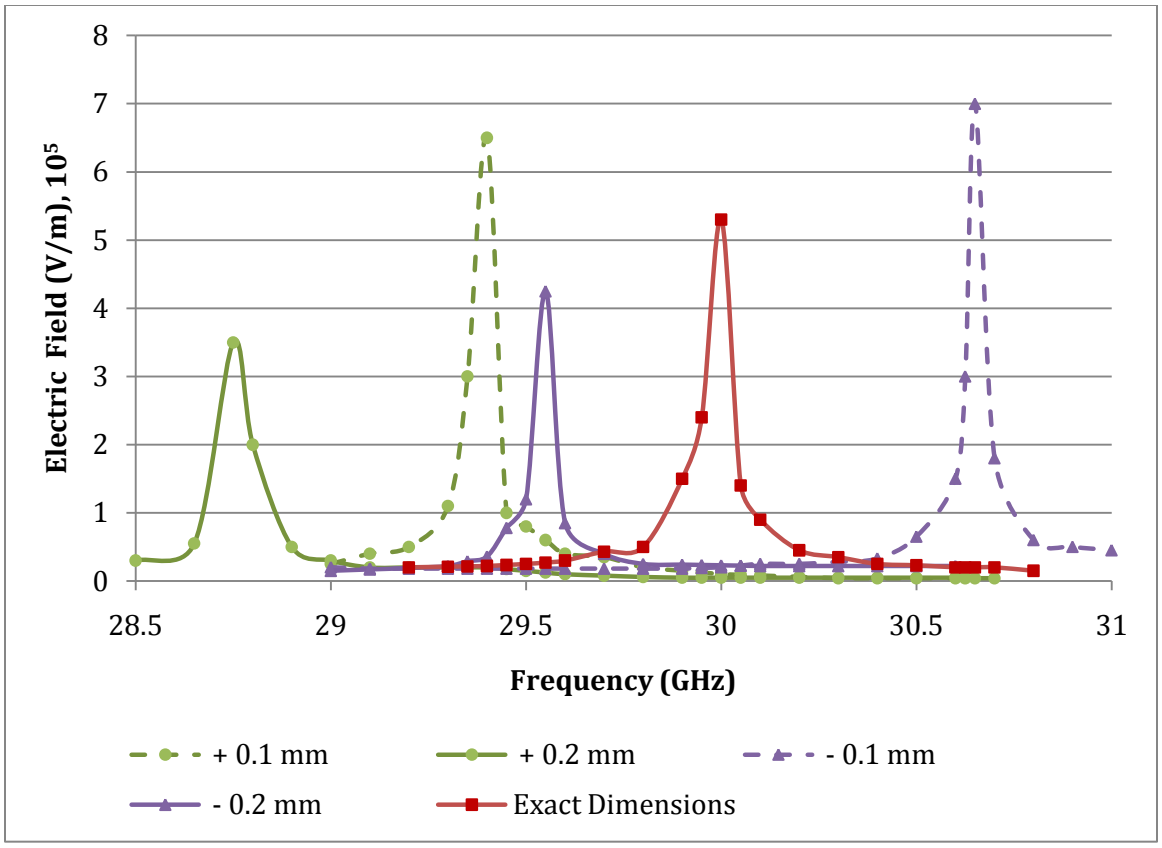

Figure 4.11: Electric Field Strength vs. Frequency for the Exact Radius, ±0.1 mm, and ±0.2 mm.

For the exact radius case, the resonant frequency is 30 GHz and has electric field strength of 5.3×10^5 V/m. The peak electric field strength and frequency changed in all four cases. For the +0.1-mm cavity, the peak electric field increased to 6.5×10^5 V/m, but the frequency also shifted down to about 29.4 GHz. The −0.1-mm cavity increased the electric field strength to 7×10^5 V/m, but increased the resonant frequency to 30.6 GHz. The +0.2-mm cavity decreased the frequency to 28.75 GHz and decreased the intensity to 3.5×10^5 V/m. The −0.2-mm cavity decreased the frequency to 29.5 GHz and decreased the electric field strength to 4.25×10^5 V/m.

From this analysis, it is concluded that variations in cavity radius on the order of 0.1 to 0.2 mm are significant. The variations impact both the electric field intensity at the nozzle entrance and the resonant frequency of the cavity. For the simulated geometries, the peak electric field occurred within 50 MHz of the resonant frequency and quickly dropped off.

CHAPTER 5

EXPERIMENTAL SETUP AND TESTING

The 30-GHz MET was designed with the goal of igniting a plasma inside of the thruster. In order to accomplish this, a propellant control system, an electromagnetic control system, and a pressure measurements control system are needed in addition to the thruster (MET system). An explanation of the equipment and setup for the MET system, propellant control system, electromagnetic control system, and the pressure measurements control system are found in this chapter.

5.1 MET System

The MET system consists of the thruster and the antenna to waveguide connection. The top and bottom plates of the thruster have an O-ring seal to the body of the cavity, which is compressed by #5-40 bolts. A pressure transducer adapter was fabricated to connect the pressure transducer to the cavity. The adapter is sealed to the cavity body with an O-ring. A propellant feed adapter was machined to connect the propellant line to the cavity. The adapter is sealed to the cavity body with epoxy. A fiber-optic was placed in one side of the cavity so that plasma generation could be verified and is sealed in place with epoxy. These features of the thruster are shown in Figure 5.1.

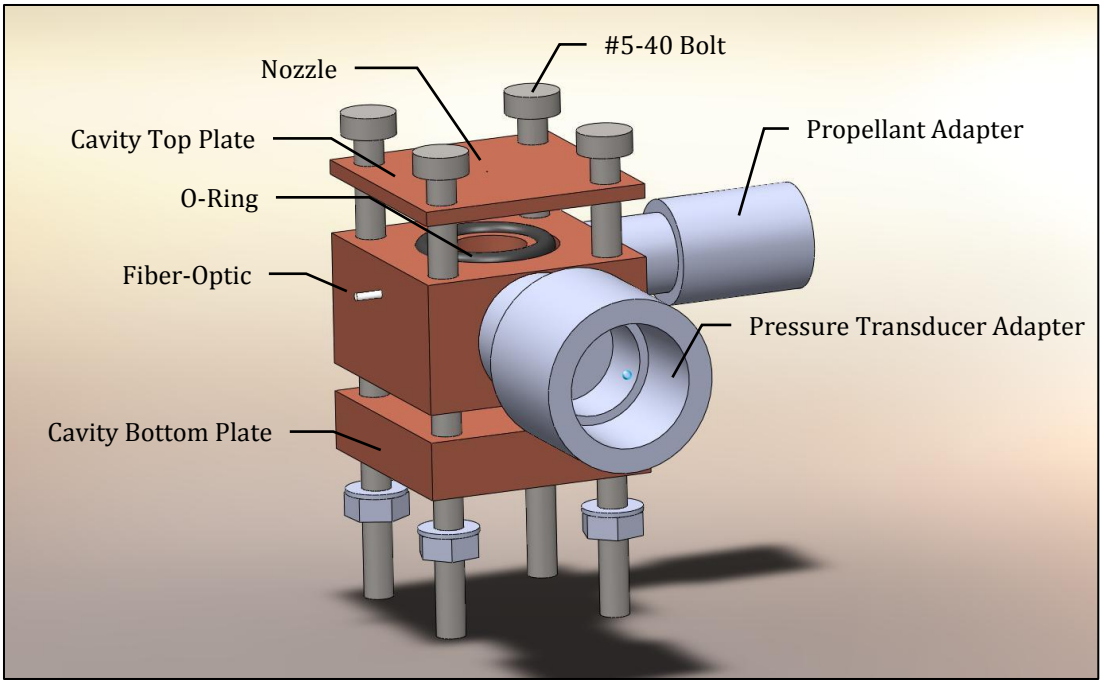

Figure 5.1: Features of the 30-GHz MET.

The antenna enters through the bottom plate of the cavity and is held in place with four #3-48 bolts. In order to connect with the electromagnetic control system, the antenna needs an adapter that goes from a female 2.4-mm connector to a WR-28 waveguide. The WR-28 waveguide adapter has female SMA threads so a transition to SMA is required. First an adapter is needed to go from 2.4-mm male threads to SMA threads. The available adapter at the time had female SMA threads. A male SMA to male SMA adapter was utilized to connect the female SMA to female SMA. These transitions are shown in Figure 5.2.

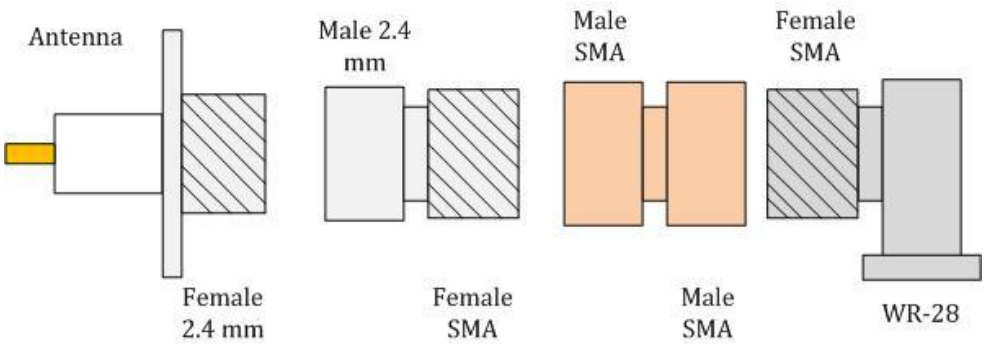

Figure 5.2: Transition from Antenna Connector to WR-28 Waveguide.

5.2 Propellant Control System

The propellant control system provides the propellant to the thruster. During initial testing, helium was used as the propellant. The control system consists of the following parts:

1. Propellant Feed Line: Copper Piping and Plastic Tubing
2. Swagelok Quarter Turn Plug Valve
3. UNIT Instruments Mass Flow Controller, UFC-8100
4. UNIT Instruments Mass Flow Control Box, URS-20
5. Helium Tank
6. Swagelok Fittings

A schematic of the propellant control system is shown in Figure 5.3.

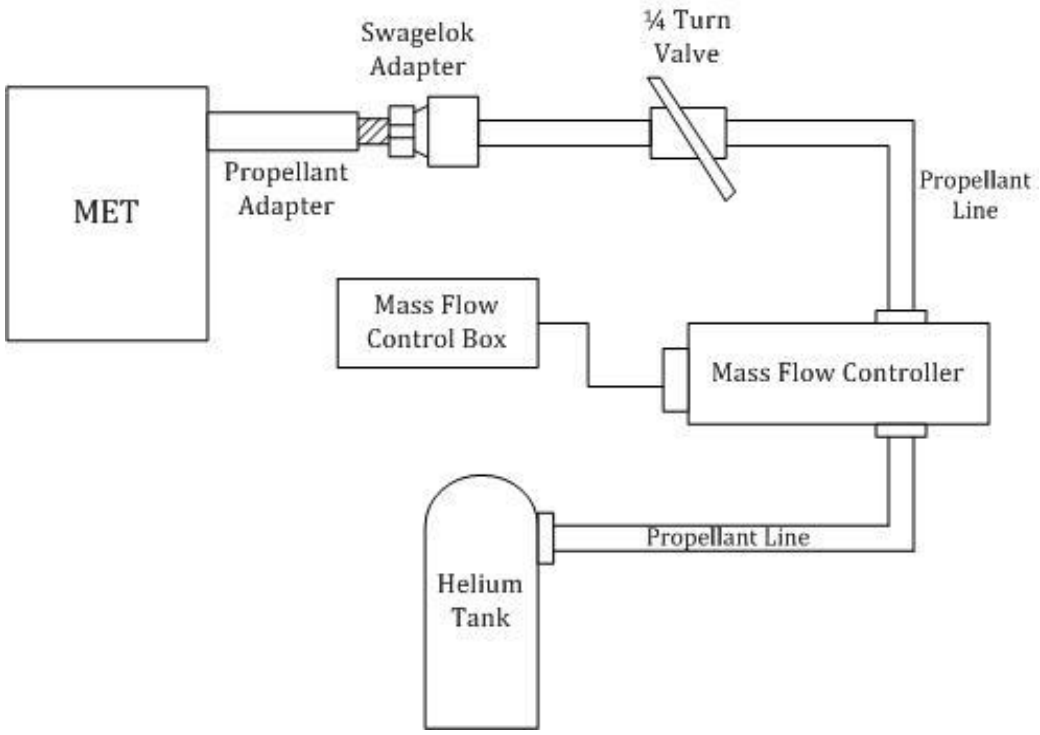

Figure 5.3: Propellant Control System Schematic.

5.3 Electromagnetic Control System

The electromagnetic control system transfers the microwave energy from the microwave source into the MET cavity. The list of equipment used for the 30-GHz MET electromagnetic control system is as follows:

1. 30 GHz Programmable Sweep Generator, Model 6640A-5
2. Hughes 8001H Traveling Wave Tube Amplifier
3. WR-28 Waveguides
4. Hughes Isolator
5. 2 – Uni-Directional 20-dB Couplers
6. 2 – 30 GHz R8486A HP Power Sensors
7. 2 – 437B HP Power Meters

The schematic of the control system is shown in Figure 5.4.

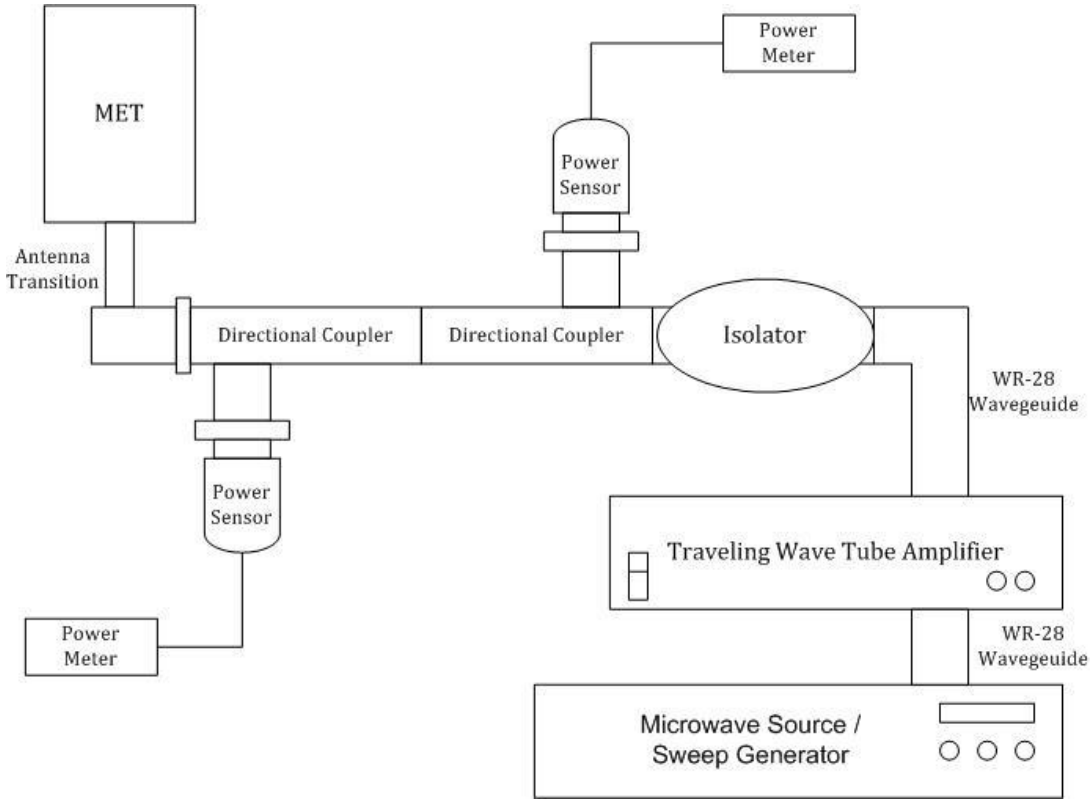

Figure 5.4: Electromagnetic Control System Schematic.

5.4 Pressure Control System

The pressure control system is used to determine the pressure inside of the cavity and to pull a partial vacuum on the cavity to aid in plasma ignition. The pressure control system consists of the following equipment:

1. Welch 1402 Duoseal Vacuum Pump
2. Pressure Lines: Aluminum Piping and Plastic Tubing
3. Vacuum Cap, 6061 Aluminum
4. 999 Quattro MKS Pressure Transducer
5. Kurt J. Lesker KPDR900 Series Pressure Meter

The schematic of the pressure control system is shown in Figure 5.5.

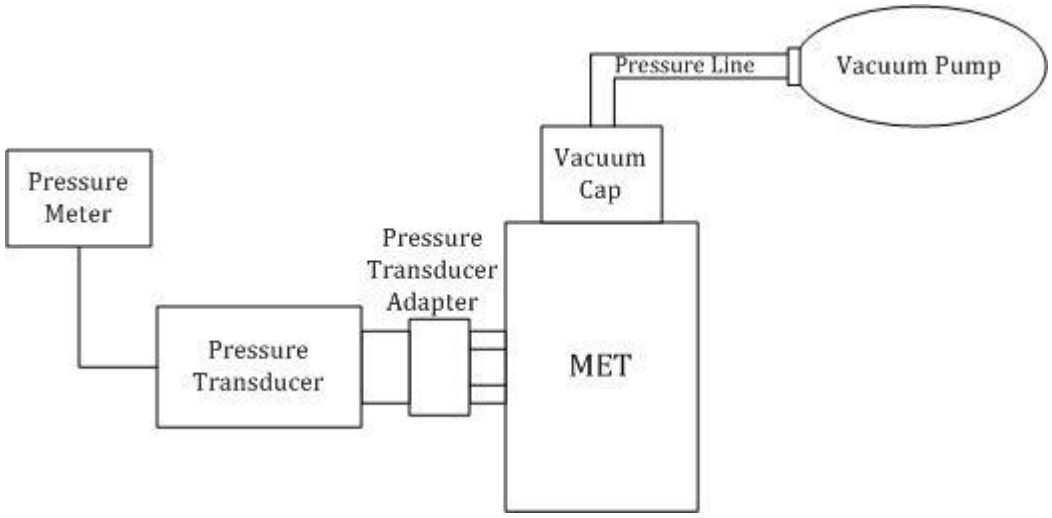

Figure 5.5: Pressure Control System Schematic.

5.5 Preliminary Testing

With the thruster fabricated and the experimental setup completed, preliminary testing of plasma ignition in the 30-GHz MET began. The maximum power available from the microwave source and TWTA is 2.94 watts. This is less than the expected amount of power needed to generate a plasma but a higher powered source was not available. For the

preliminary testing, the antenna length was not reduced to 0.0 mm and instead was left at its manufactured length of 1.78 mm. The length was left intact with the idea that it is easier to remove excess length later than it is to add the antenna length back.

In order to ignite a plasma, cavity pressure must reach at least 30 Torr. This pressure has been difficult to obtain due to a pressure leak through the center part of the antenna. The pressure leak through the antenna has prevented pressures below 80 Torr. An alternative antenna transition was used to attempt to stop the leak but has proven to be erratic. It was noted that when the antenna transition was under bending stress, the leak was sealed. In this position, testing commenced to attempt to ignite a plasma at 30 GHz with 2.94 watts, a pressure of 30 Torr, and an antenna length of 1.78 mm. The experimental setup for the preliminary testing can be seen in Figure 5.6. A close-up of the experimental setup for the thruster is shown in Figure 5.7.

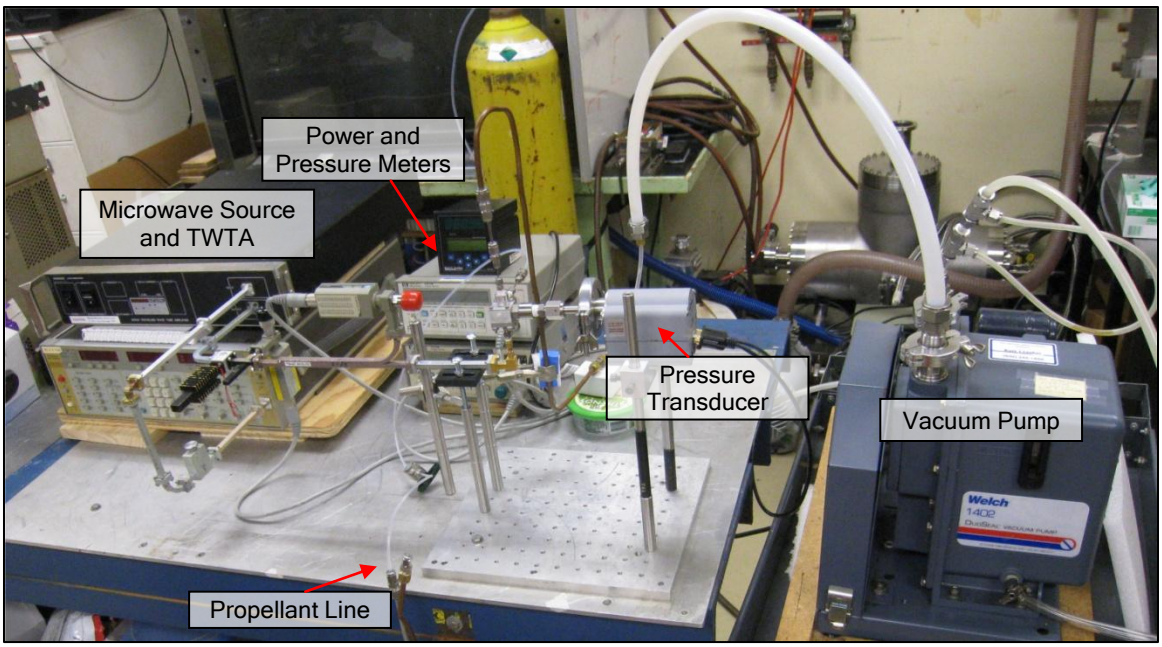

Figure 5.6: Experimental Setup Used for Preliminary Testing.

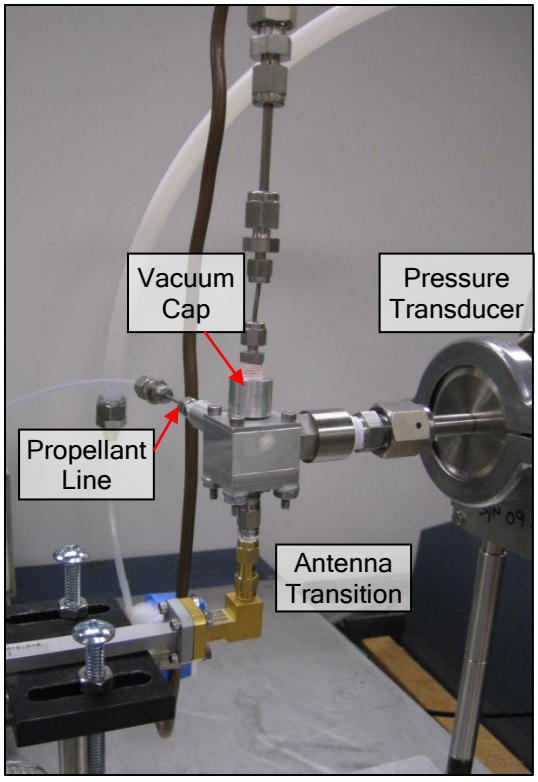

Figure 5.7: Experimental Setup of the 30-GHz Thruster Used for Preliminary Testing.

The vacuum cap was placed on the cavity and the pressure transducer was turned on and read atmospheric pressure. The propellant line was opened and the cavity was flushed with helium for two minutes. This was performed with the hopes of only having helium in the cavity when the testing commenced as it is easier to breakdown than air. The propellant line was closed with the valve and the vacuum pump turned on. Once cavity pressure reached about 30 Torr, the microwave source was switched from stand-by mode to operate mode. There were 2.94 watts of incident power and about 1.6 watts of reflected power. This resulted in less than 50% power coupling to the cavity and, as such, plasma ignition did not occur. The lack of available power, the cavity's exact resonant frequency, and potentially the length of the antenna may have prevented ignition.

From the computational results in Section 4.3, it was noted that machining precision of the cavity is very important. Because of the machining precision required, there is the possibility that the resonant frequency of the cavity is not exactly 30 GHz, which will also affect the ability to ignite a plasma. The thruster was connected to a vector network

analyzer (VNA) to determine the exact resonant frequency of the cavity. The results from the network analyzer with the cavity and antenna are shown in Figure 5.8.

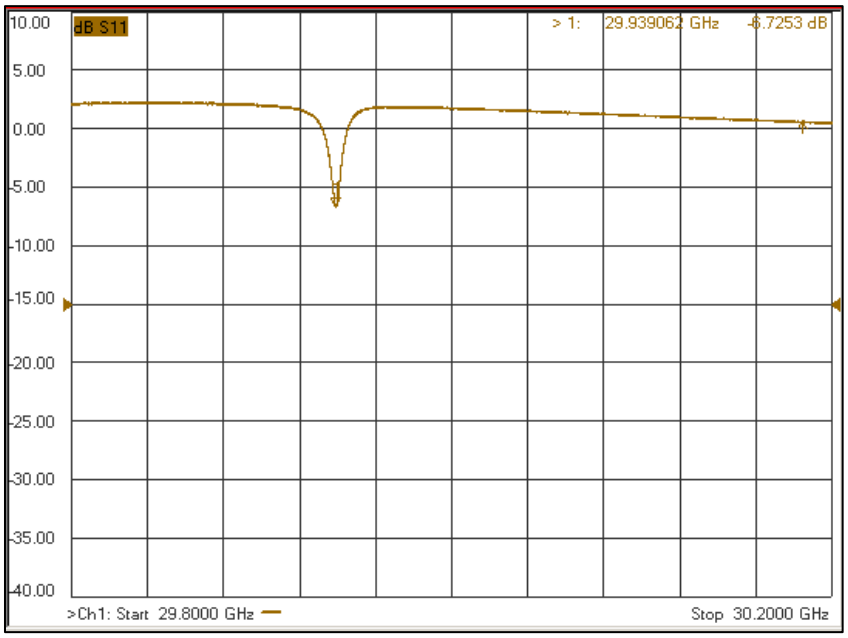

Figure 5.8: Network Analyzer Results for the 30-GHz MET Indicating Power Coupling.

The VNA measurement indicates that the actual resonant frequency of the cavity is 29.939 GHz. At this frequency with the 2.4-mm antenna and an antenna length of 1.78 mm, the power coupling was about 6 dB. This coupling is not sufficient for plasma ignition.

As discussed in Section 4.2, the antenna length directly impacts the power coupling to the cavity as well. The antenna was pulled out slightly from the cavity, producing the effect of a shorter antenna. This resulted in much better power coupling. The VNA measurement for this shorter antenna configuration is shown in Figure 5.9.

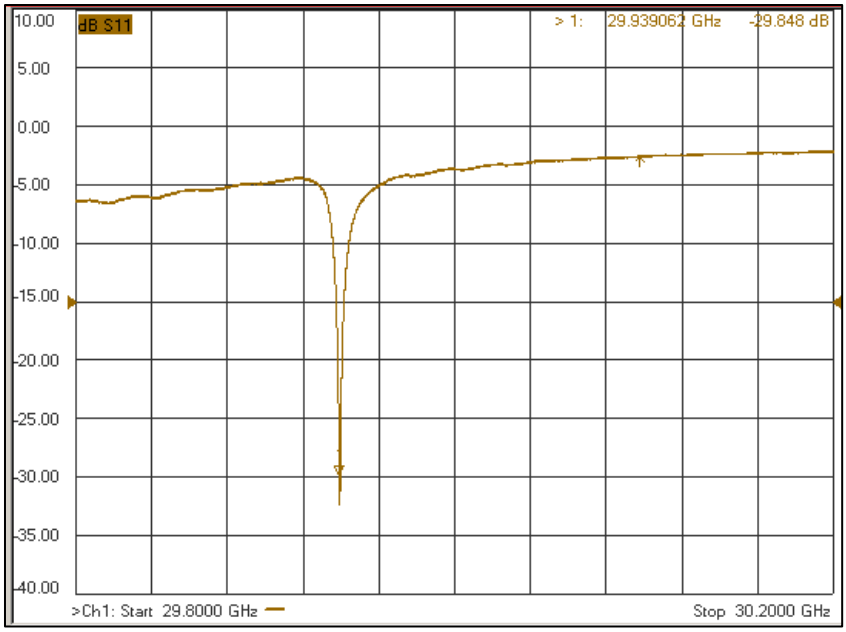

Figure 5.9: Network Analyzer Results with a Shorter Antenna Length.

The results of this test show a power coupling of about 25 dB at a frequency of 29.939 GHz. The network analyzer results support the computational results of an optimal length to the antenna. The next step will be to systematically test different antenna lengths on the network analyzer until an optimal length resulting in power coupling of at least 30 dB is obtained. Results from the network analyzer have also provided the exact resonant frequency of the cavity. This resonant frequency will also aid in igniting a plasma in the future.

CHAPTER 6

CONCLUSION AND RECOMMENDATIONS

The 30-GHz Microwave Electrothermal Thruster (MET) is a product of 20 years of research at The Pennsylvania State University. Beginning with the 2.45-GHz MET, research has shown that with increased frequency, the MET can ignite and sustain a plasma at lower input powers. The goal of the 30-GHz MET is to provide propulsion that requires less input power than other similar forms of propulsion. The higher frequency results in a physically smaller thruster, while consuming less power results in a power supply with less mass. The thruster is ideal for use on CubeSats where space is limited and a light-weight propulsion system can expand mission capabilities.

This thruster was designed to operate at 30 GHz and in the TM_{011}^{z} mode. In order for the thruster to have a resonant frequency of 30 GHz, the necessary dimensions of the thruster cavity were a radius of 0.40857 cm and a height of 1.4299 cm. The cavity is cylindrical and has a conducting plate on each of the ends, one for the antenna entrance and one for the nozzle. During testing the thruster required a vacuum cap to provide a simulated vacuum environment to discharge the nozzle exhaust. Various O-rings were used for sealing connectors to the cavity and epoxy was used in the areas where O-rings were not effective. Initial testing is being performed using helium as the propellant which enters the cavity via a propellant feed located near the nozzle entrance. A fiberoptic is used to visually confirm plasma generation during testing.

Using COMSOL Multiphysics, the thruster was modeled to determine the optimal antenna type, antenna length, and the importance of accurate machining of the cavity's radius. The modeling resulted in the selection of a 2.4-mm antenna with a length that is flush with the bottom of the cavity. By varying cavity sizes in COMSOL, it was determined that the machining of the cavity radius must be as close as possible to 0.40857 cm. Inaccuracies on the order of ±0.1 mm resulted in poor power transfer to the cavity, low electric field strength, shifted resonant frequency, and mode distortion.

Once the fabrication of the thruster and the experimental setup was complete, preliminary testing commenced. Initial testing was at 30 GHz with an input power of 2.94 watts and a cavity pressure of 30 Torr. A 2.4-mm antenna with a length of 1.78 mm was used. Initial testing did not result in plasma ignition. The thruster was placed on a network analyzer to determine the cavity's exact resonant frequency and to analyze the power coupling. The results indicate that the resonant frequency is exactly 29.939 GHz and the power coupling can be improved by reducing the antenna length.

While fabricating, assembling, and testing the thruster, a number of design improvements were noted and should be considered in any future redesign of the thruster. First, the #8-32 thread size used for the pressure transducer and propellant feed should be changed to a VCO O-ring face seal. A VCO O-ring face seal to NPT Swagelok adapter should be used for the pressure transducer assuming the pressure transducer used has an NPT connection. The propellant feed would need either a VCO O-ring face seal to tube Swagelok adapter or a VCO O-ring face seal to SAE/MS Swagelok adapter. Both connectors would provide the necessary sealing to the cavity and the correct connection to the propellant lines. For either type of connector, it may be a problem that the commercially available adapters are physically too large to fit on the side of the thruster. If this is the case, the outer walls of the thruster would need to be modified to accommodate the adapters. This design change would help tremendously with sealing the cavity. While the suggested adapter for the pressure transducer would be ideal for the current pressure transducer, a smaller pressure transducer would help with the setup of the experiment. Currently, the pressure transducer is large enough that the connection between the two is fragile and the setup is tedious.

An improvement is currently underway to replace the antenna transition with a hermetically sealed version. In order to achieve the pressure required to ignite a plasma, a hermetically sealed antenna transition is required. Leaks through the center of the current antenna transition are significant and cannot be eliminated in any other way. Prior METs have had issues with plasma formation near the antenna resulting in antenna damage; therefore, it may be necessary in the future to include a dielectric plate in this thruster to prevent plasma formation near the antenna. Lastly, alternatives to the fiber optic, used for visual confirmation of plasma ignition, should be explored. The epoxy required to seal it in

place results in an unkempt thruster exterior. As a rule of thumb, epoxy should be avoided when possible since it is intended to be permanent.

REFERENCES

1. Hill, P. G., and Peterson, C. R., *Mechanics and Thermodynamics of Propulsion*, Addison-Wesley Publishing Company, Inc., 1965.

2. Jahn, R. G., *Physics of Electric Propulsion*, Dover Publications, Inc., New York, 1996.

3. Janson, S. W., Crofton, M. W., Welle, R. P., Pollard, J. E., and Cohen, R. B., "The Physics and Chemistry of Radio Frequency and Microwave Thrusters," AIAA-1991-1501-195, 1990.

4. Whitehair, S., Asmussen, J., and Nakanishi, S., "Microwave Electrothermal Thruster Performance in Helium Gas," *Journal of Propulsion and Power*, 1986.

5. Balaam, P., and Micci, M., "Investigation of Free-Floating Nitrogen and Helium Plasmas Generated in a Microwave Resonant Cavity," AIAA-89-2380, 25th AIAA/ASME/SAE/ASEE JPC, 1989.

6. Mueller, J., *Performance Evaluation and Operating Characteristics of a Waveguide Microwave Applicator for Space Propulsion Applications*, Ph.D. Dissertation, The Pennsylvania State University, 1993.

7. Balaam, P., *The Experimental Development of a Microwave Resonant Cavity Electrothermal Thruste*r, Ph.D. Dissertation, The Pennsylvania State University, 1997.

8. Sullivan, D. J., *Development and Performance Characterization of a Microwave Electrothermal Thruster Prototype*, Ph.D. Dissertation, The Pennsylvania State University, 1995.

9. Nordling, D. A., *High-Frequency Low Power Microwave Arcjet Thruster Development*, M.S. Thesis, The Pennsylvania State University, 1998.

10. Souliéz, F. J., *Low-Power Microwave Arcjet Spectroscopic Diagnostics and Performance Evaluation*, M.S. Thesis, The Pennsylvania State University, 1999.

11. Clemens, D. E., *Performance Evaluation of a Low-Power Microwave Electrothermal Thruster*, M.S. Thesis, The Pennsylvania State University, 2004.

12. Goovaerts, K. M., *Feasability Studies of a 14.5-GHz, Low Power Microwave Electrothermal Thruster*, M.S. Thesis, The Pennsylvania State University, 2007.

13. Adusumilli, R. P., *Performance Evaluation and Optimization of High Power 14.5-GHz Miniature Microwave Electrothermal Thruster*, M.S. Thesis, The Pennsylvania State University, 2011.

14. Blum, J. H., *Performance Evaluation and Optimization of an 8-GHz Microwave Electrothermal Thruster*, M.S. Thesis, The Pennsylvania State University, 2009.

15. Bilén, S. G., Valentino, C. J., Micci, M. M., and Clemens, D. E., "Numerical Electromagnetic Modeling of a Low-Power Microwave Electrothermal Thruster," AIAA-2005-3699, 41st AIAA/ASME/SAE/ASEE JPC, 2005.

16. Valentino, C. J., *A Numerical Study of a Microwave Electrothermal Thruster*, M.S. Thesis, The Pennsylvania State University, 2007.

17. DeForce Jr., C. A., *Computational Modeling of an 8-GHz Microwave Electrothermal Thruster*, M.S. Thesis, The Pennsylvania State University, 2011.

18. Balanis, C. A., *Advanced Engineering Electromagnetics*, John Wiley & Sons, Inc., Hoboken, 1989.

19. Pozar, D. M., *Microwave Engineering*, 3rd Edition, John Wiley & Sons, 2005.

20. Chen, F. F., *Introduction to Plasma Physics and Controlled Fusion*, 2nd Edition, Plenum, New York, 1984.

APPENDIX

THRUSTER DESIGN DRAWINGS

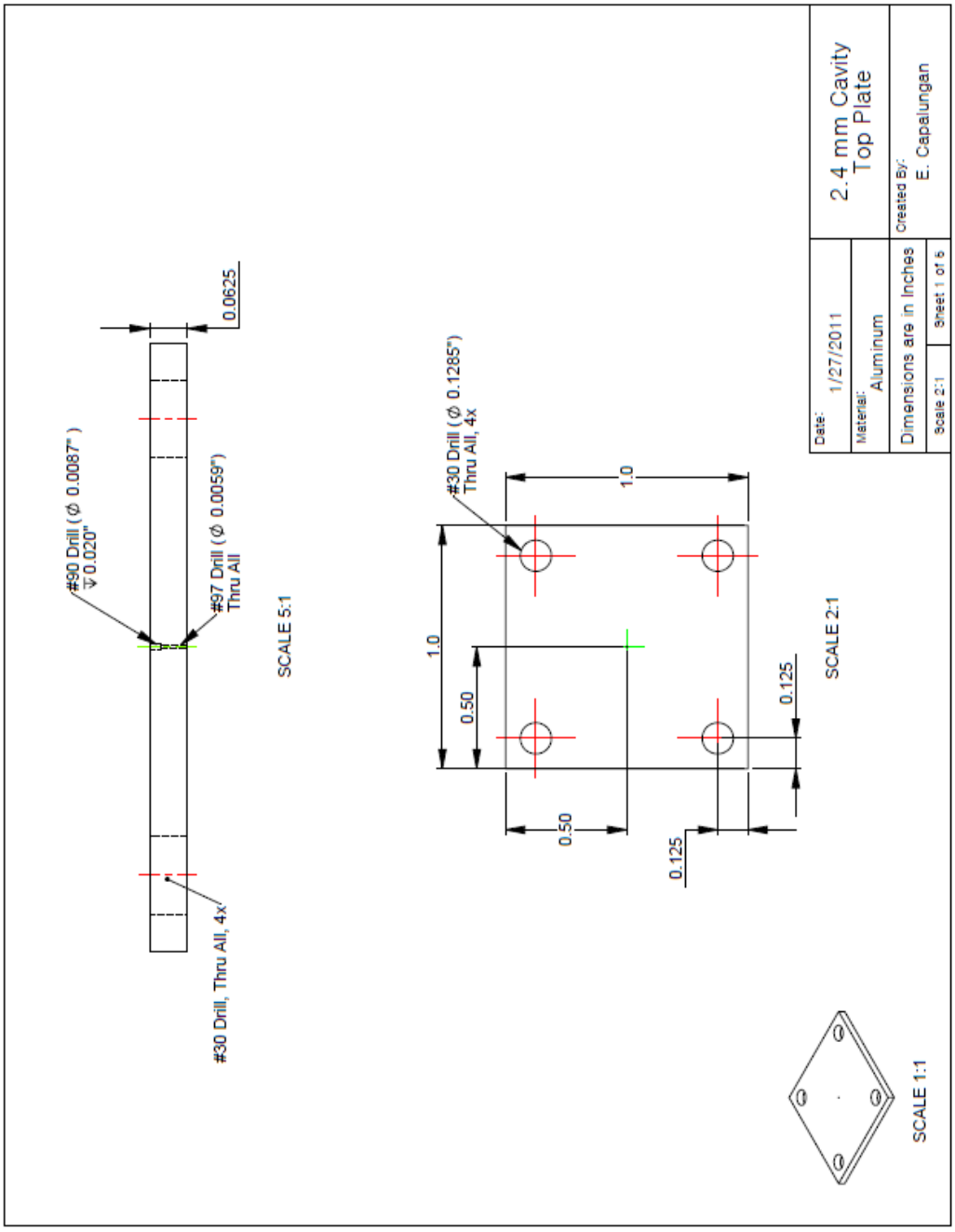

Figure 0.1: Drawing of Cavity Top Plate.

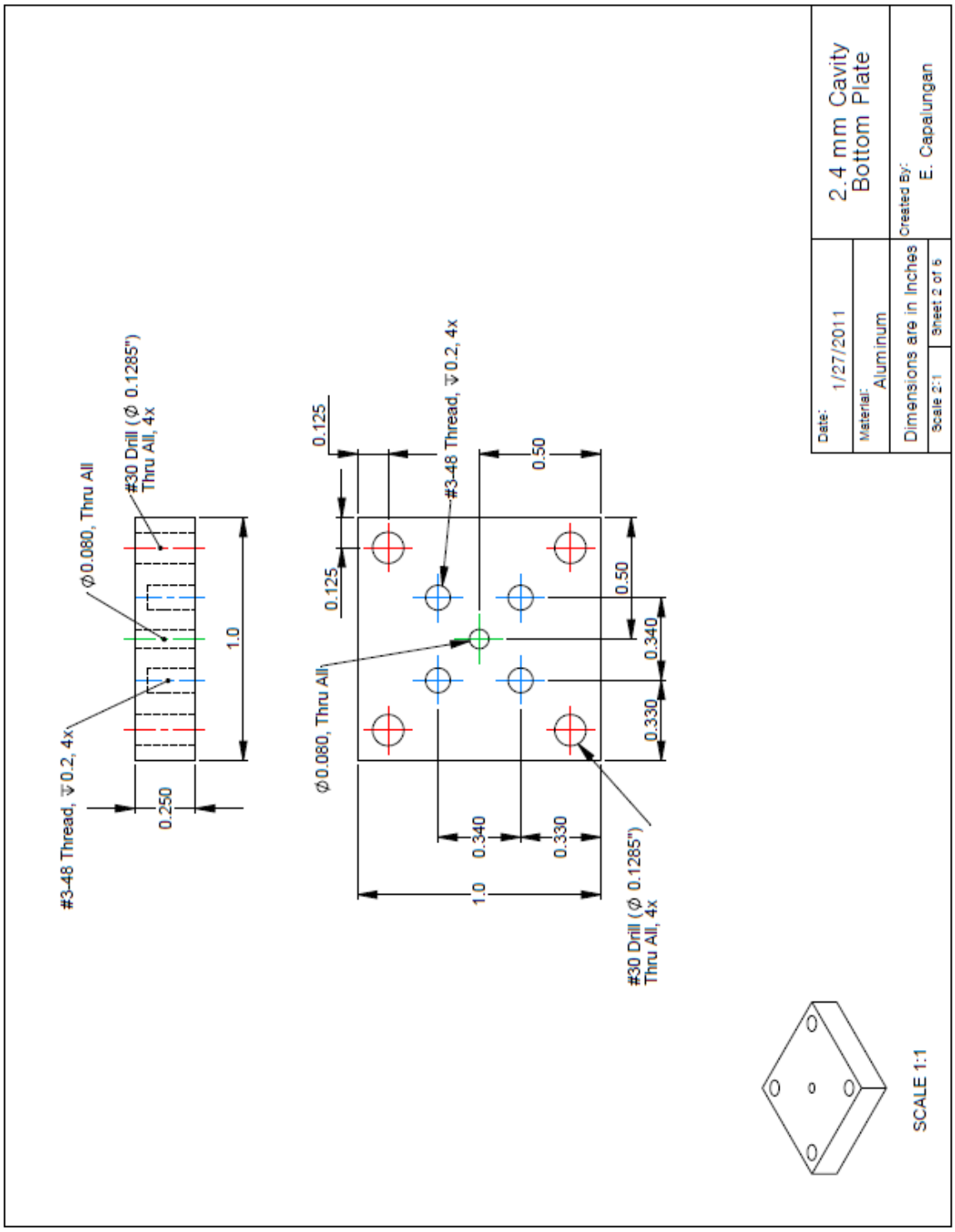

Figure 0.2: Drawing of Cavity Bottom Plate.

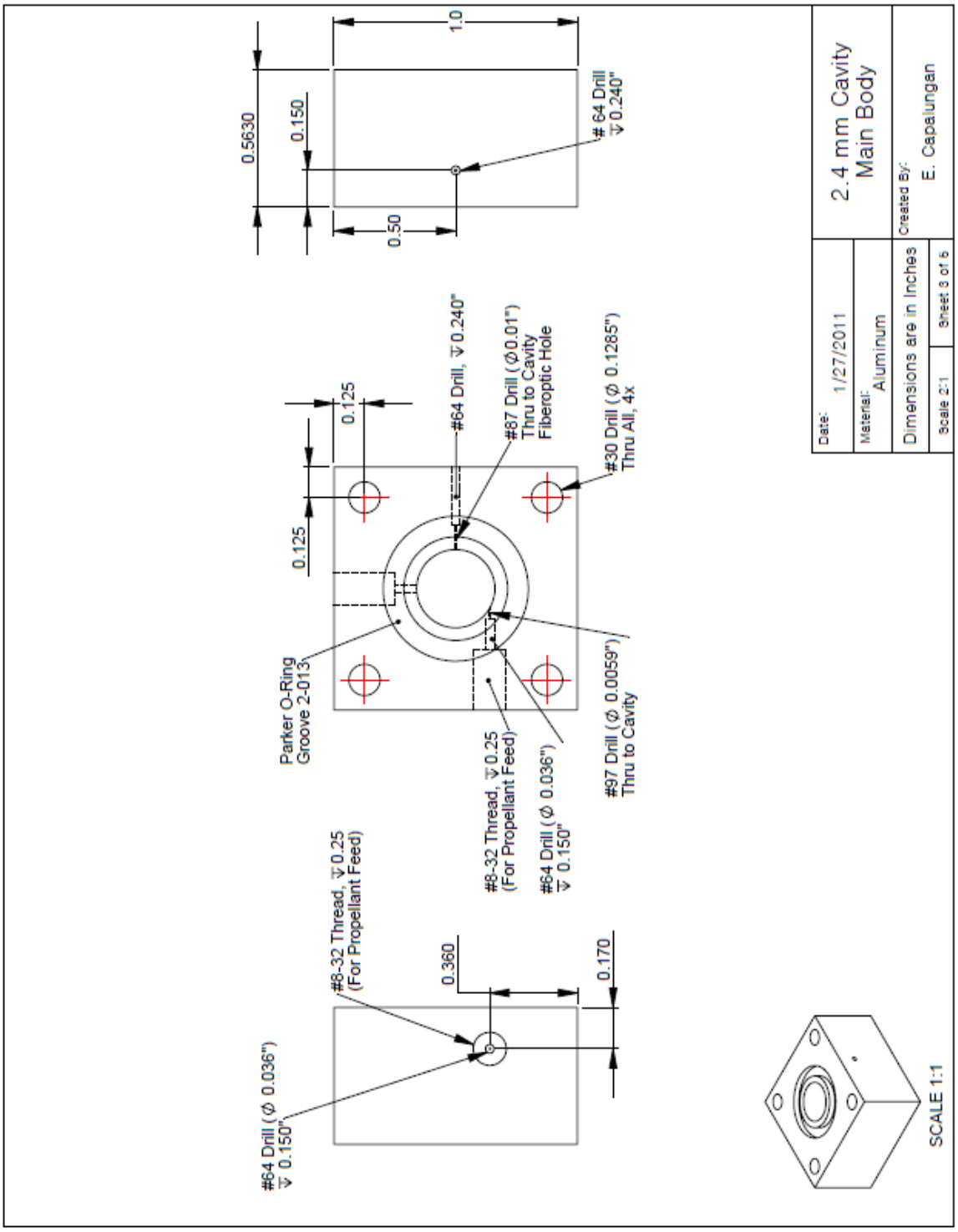

Figure 0.3: Drawing of Cavity Main Body, View 1.

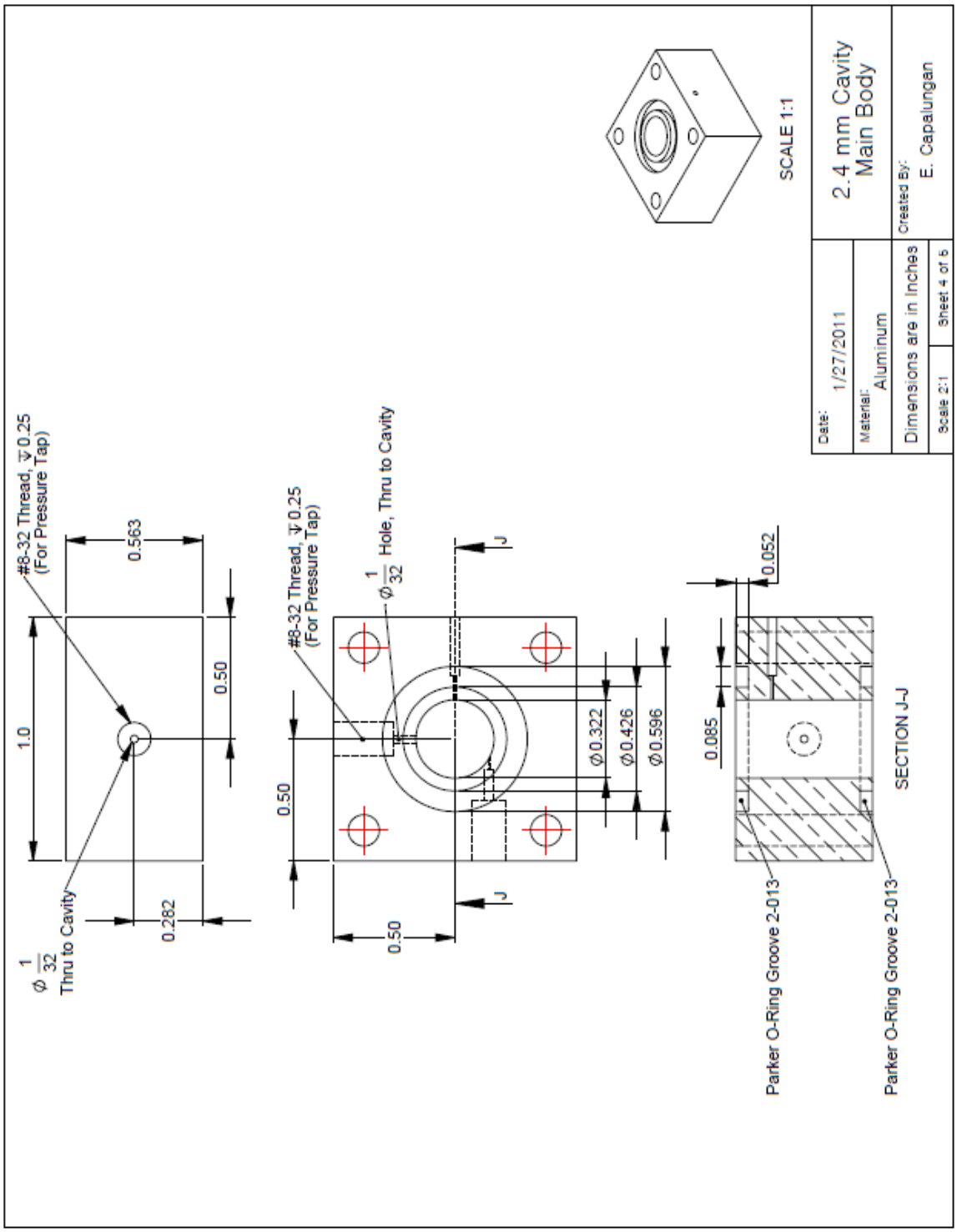

Figure 0.4: Drawing of Cavity Main Body, View 2.

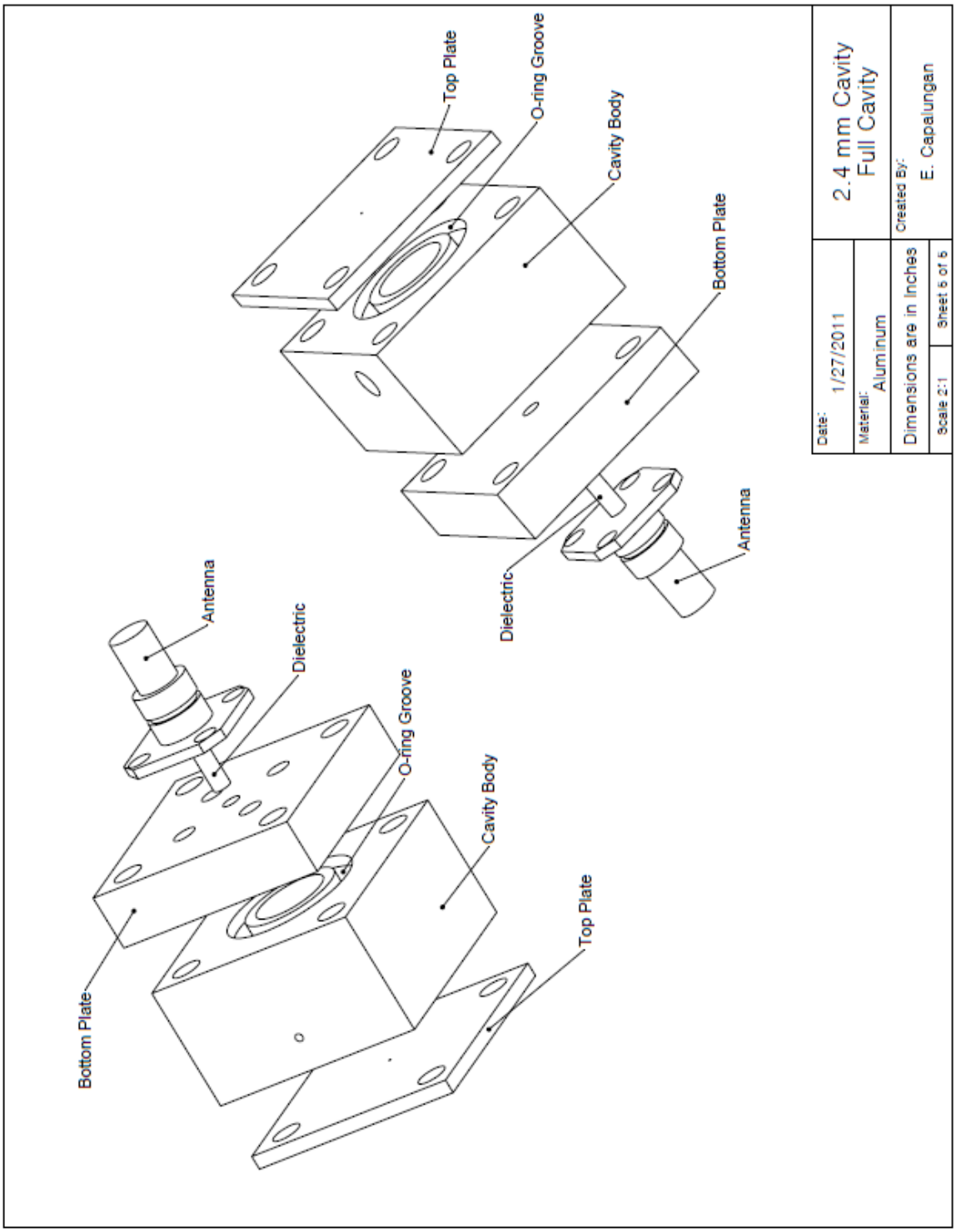

Figure 0.5: Assembled Cavity with Antenna.

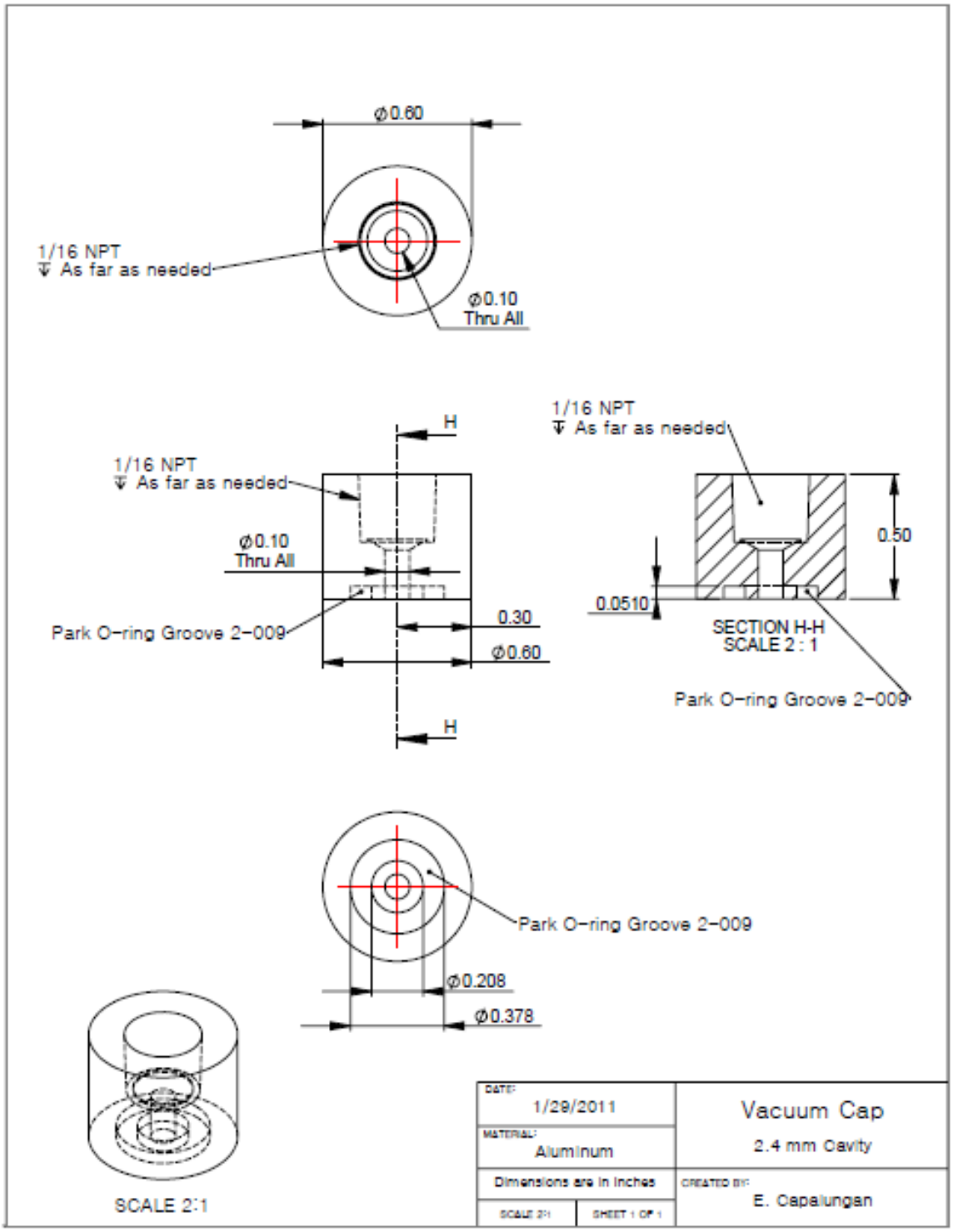

Figure 0.6: Drawing of Vacuum Cap Attachment.

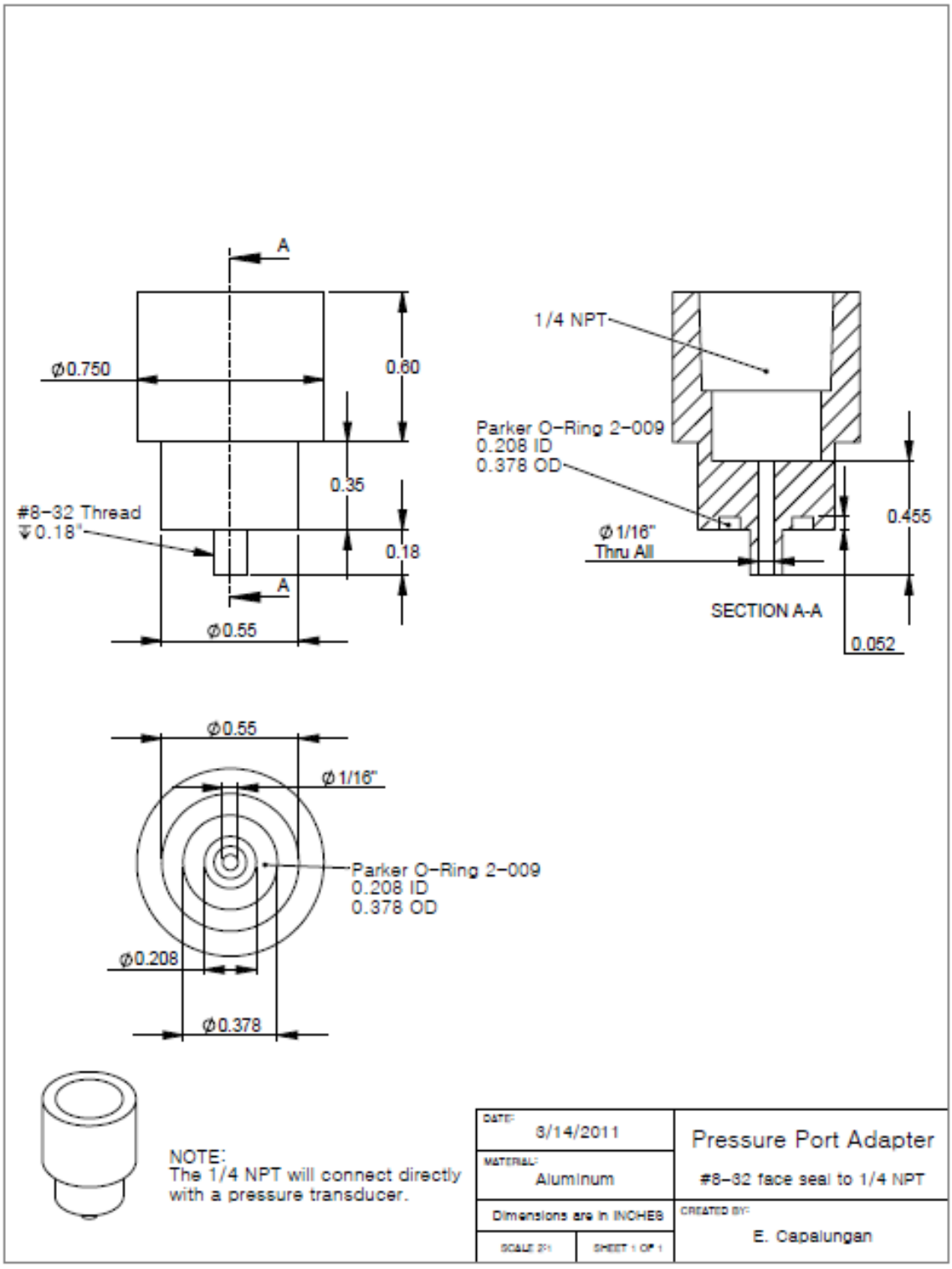

Figure 0.7: Drawing of Pressure Port Adapter.

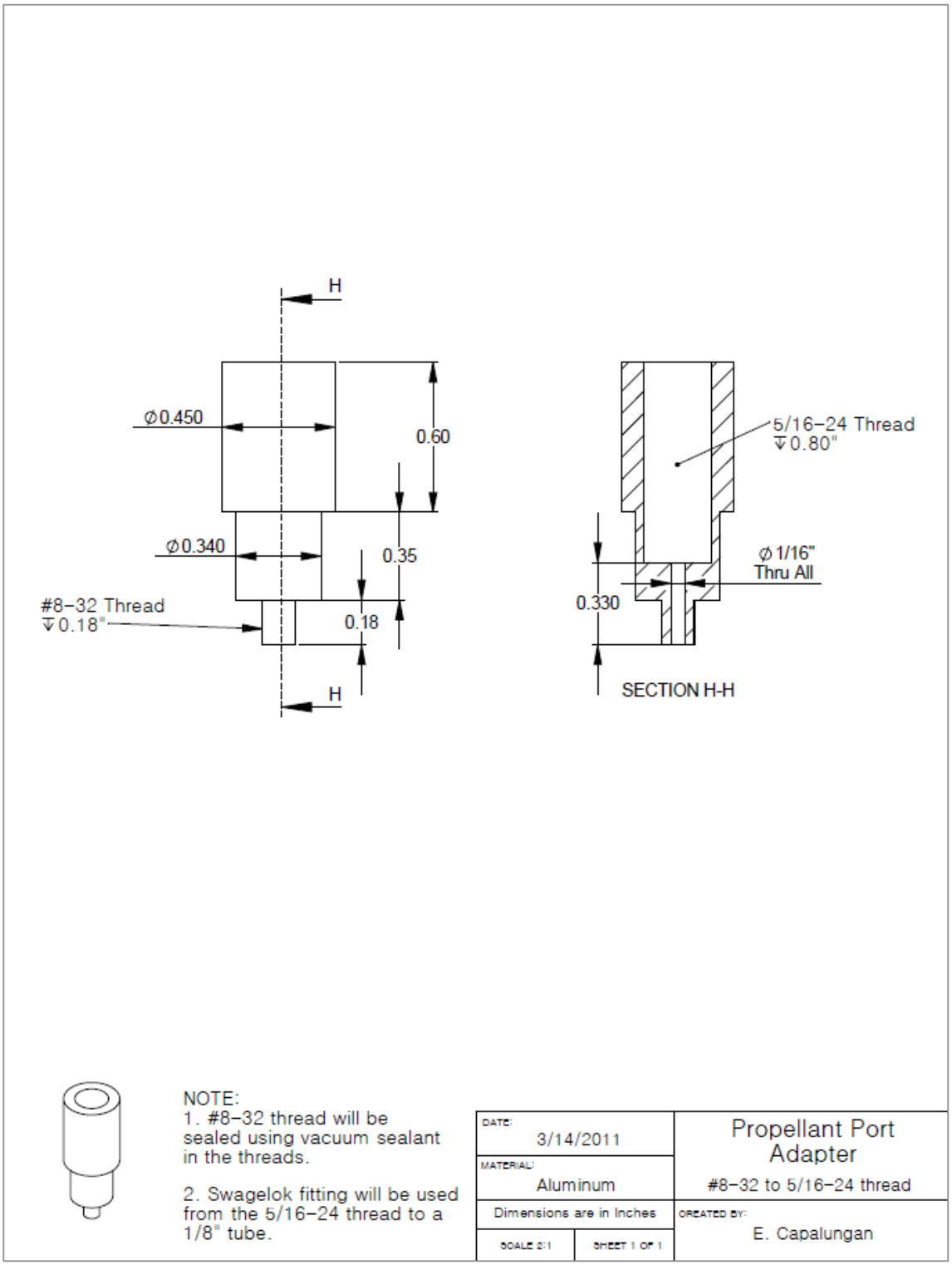

Figure 0.8: Drawing of Propellant Port Adapter.